Data repository for `Active normal fault control on landscape and rock-slope failure in northern Norway´

By

Osmundsen, P.T.[1] & Henderson, I.[1] , Lauknes, T. R.[2], & Larsen, Y.[2], Redfield, T.F.[1] & Dehls, J.[1]

1: Geological Survey of Norway, 7491, Trondheim, Norway 2: Norut a/s, Forskningsparken, 9294 Tromsø, Norway

Data Repository (DR) item 1: Geological map of part of northern Scandinavia between Lyngen and Lofoten and adjacent offshore areas (Mainly from Sigmond 2002).

The geology of onshore northern Scandinavia is dominated by remnants of the Caledonian Mountain belt (Proterozoic and younger rocks) and by the Archean to Proterozoic rocks of the Baltic shield (Fig. 1.1). West of the Caledonian nappe front, gneissic rocks, belonging to the Baltic shield or to structurally low allochthonous units, crop out in belts and windows. The gabbros, greenstones and ultramafics of the Lyngen Ophiolite belong to the Caledonian nappe succession occupy large parts of the Lyngen peninsula. Compared to surrounding, penetratively foliated schistose units, the ophiolite consists of relatively resistant rocks. However, high topography is not confined to the Lyngen ophiolite, and across southern Lyngenfjorden, the contrast in topographic elevation is relatively small. A pronounced marker is constituted by the so-called `summit surface´, an undated palaeosurface incised into ophiolitic rocks as well as in the surrounding schists (see main text and data repository item 4). On the map, please note the NE-SW to NNE-SSW-trending fault systems that constitute the boundary between the continent and the offshore Mesozoic-Cenozoic Harstad Basin. The trend of the bounding faults is reflected by the trends of a number of onshore faults, by a number of fjords and valleys and by the NNE-SSW orientation of the Lyngen peninsula. The main active faults proposed by us to bound the Lyngen peninsula (marked in red on fig. 1.1.) are thus parallel to major faults that offset offshore stratigraphy.

Reference:

Sigmond, E.M.O., 2002. *Geologisk kart over land- og havområder I Nord-Europa, målestokk 1:4 millioner*. Norges geologiske Undersøkelse.

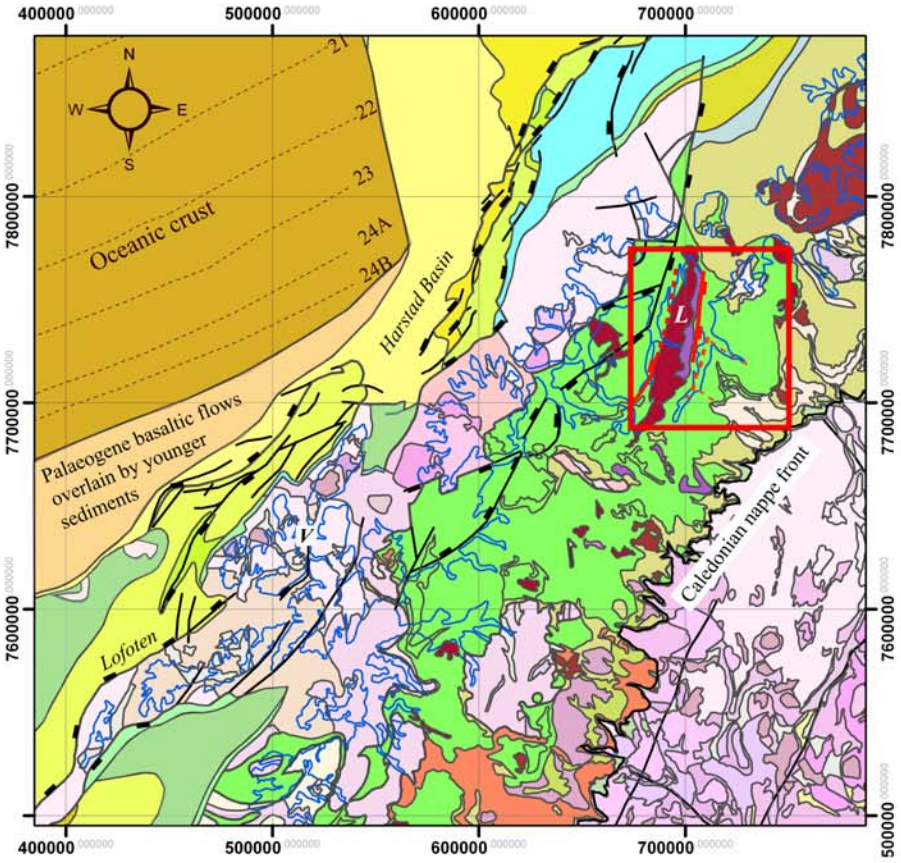

Offshore:

- Pliocene sandstone, siltstone and claystone
- Palaeocene-Eocene claystone and diatomite, sandy ash layers, subordinate limestone, dolomite
- Late Cretaceous limestone, marl, mudstone, sandstone, conglomerate, chalk
- Early Cretaceous sandstone, siltstone, mudstone, chalk
- Jurassic limestone, sandstone, siltstone and mudstone
- Triassic sandstone, siltstone, claystone,
- Mid Carboniferous - Permian carbonates, sandstone, claystone, gypsum
- Early Carboniferous claystone, siltstone, sandstone and greywacke

Onshore:

- Ordovician gabbro, diorite, peridotite, amphibolite (mainly Lyngen Ophiolite), Proterozoic-Cambrian mafics and ultramafics
- Cambrian-Ordovician greenstone and greenschist
- Proterozoic and Palaeozoic micascist, phyllite, mica-rich gneiss, metasandstone
- Proterozoic gneiss, migmatite, granite, augengneiss
- Proterozoic metasandstones, conglomerates, carbonates, mudstone, phyllite, micaschist
- Archean and Proterozoic rocks, mainly granitic, granoidioritic and monzonitic gneiss with amphibolites and metasedimentary rocks

Fig. DR1. Geological map of part of northern Scandinavia and adjacent offshore areas. Study area outlined in red. *V* = Vesterålen, *L* = Lyngen peninsula. UTM coordinates, metres. From Sigmond, (2002).

DR item 2: INSAR Technical Notes

Description of data, processing, and inversion for deformation velocity

The interferometric synthetic aperture radar (InSAR) analysis is based on 19 European Space Agency ERS-1 and ERS-2 synthetic aperture radar (SAR) data from 1992 through 1999 (descending track 251, frame 2196). The ERS satellites have an operating wavelength of 5.66 cm, and the radar looks to the right (west) with an angle of approximately 23.5° from the vertical. The radar is only sensitive to displacement changes with a component in the radar line-of-sight direction.

We computed 59 interferograms (see Table 1.**)** with a maximum baseline of 450 m and a maximum temporal separation of 5 years using the Norut GSAR software (Larsen et al., 2005). A digital elevation model (DEM) with a grid size of 25x25 m and a height standard deviation of 5–6 m was used to remove the topographic phase. Only snow-free SAR scenes were used in the study. We applied a complex multi-look operation using two looks in range and eight looks in azimuth, producing pixels with ground range dimensions of about 50x30 m in the range and azimuth directions, respectively.

For each complex interferogram, a best fitting linear phase ramp due to imprecise orbit knowledge was estimated and removed (Lauknes et al., 2005). In addition, after removal of the orbital phase ramp, differential phase delay due to tropospheric stratification was estimated for each interferogram, assuming that phase as a function of elevation is the same for the entire scene. Based on the individual differential estimates, we solve for the phase as a function of height for each SAR scene using a least squares approach, and remove the resulting differential contribution from each interferogram. Furthermore, in order to exclude decorrelated areas from the study, and to make phase unwrapping feasible, we performed a pixel thresholding, selecting only the pixels that exhibited an estimated coherence value larger than 0.25 in at least 30% of the interferograms. The overall phase coherence is relatively high due to the limited vegetation cover above 600-700 m elevation.

In order to ease the phase unwrapping of the interferograms, a Delauney triangulation and interpolation (Costantini and Rosen, 1999) was done for all images, based on the selected pixels only. By performing this operation, we are able to link closely separated coherent patches. It

should be noted that for this particular dataset we do have coherent points all around the Lyngen fjord. The maximum width of the fjord is about 5 km. The interferograms were unwrapped using the SNAPHU software **(**Figures 1.1 to 1.5; Chen and Zebker, 2001). It can be clearly seen that our unwrapping approach is able to correctly unwrap across the fjord. It should be noted that our preprocessing steps (orbital error ramp and atmospheric stratification removal) are crucial for a successful spatial unwrapping.

After removing orbital trends and topography related atmosphere, as well as replacing the phase of low coherence points with Delauney triangulated phase, we are left with a spatially correlated atmospheric signal with at most one or two phase cycles throughout the entire scene. In addition, we have the assumed tectonic movement of a magnitude less than a phase cycle over a period of up to 5 years (the maximum temporal separation). If this assumption is true, the signal is possible to unwrap even across the fjord since an unwrapper will select the smallest possible phase difference in case of an ambiguity. In this dataset we also have coherent points all around the fjord, which helps the unwrapping procedure. After the phase unwrapping, all pixels were calibrated with respect to an arbitrary point on the eastern shore of the Lyngen fjord.

Based on the 59 InSAR pairs, we then applied the small-baseline subset (SBAS) algorithm (Berardino et al., 2002). In order to exclude decorrelated areas from the study, we selected only the common coherent pixels in all interferograms. The spatially correlated atmospheric contributions were estimated and filtered out before estimating a mean displacement velocity.

References

Berardino, P., Fornaro, G., Lanari, R., and Sansosti, E., 2002, A new algorithm for surface deformation monitoring based on small baseline differential SAR interferograms: IEEE Transactions on Geoscience and Remote Sensing, v. 40, no. 11, p. 2375–2383.

Costantini, M., and Rosen, P., 1999, A generalized phase unwrapping approach for sparse data: In Proc. IGARSS, Hamburg, Germany, p. 267–269.

Chen, C., W., and Zebker, H., A., 2001, Two-dimensional phase unwrapping with use of stastistical models for cost functions in nonlinear optimization: Journal of the Optical Society

of America A., v. 18, no. 2, p. 338–351.

Larsen, Y., Engen, G., Lauknes, T. R., Malnes, E., and Høgda, K. A., 2005, A generic differential interferometric SAR processing system, with applications to land subsidence and snow-water equivalent retrieval: In Proc. Fringe 2005 Workshop, ESA ESRIN, Frascati, Rome.

Lauknes, T. R., Dehls, J., Larsen, Y., Høgda, K. A., and Weydahl, D. J., 2005, A comparison of SBAS and PS ERS InSAR for subsidence monitoring in Oslo, Norway: In Proc. Fringe 2005 Workshop, ESA ESRIN, Frascati, Rome.

Acknowledgments

The ERS-1/2 synthetic aperture radar data were provided by the European Space Agency through proposals AOALO.3668 and AOPOL.4104. The University of Delft, The Netherlands, provided precise satellite orbits.

Table DR1.

Parameters of SAR images used in the InSAR analysis

Interferogram [dates]	Perpendicular baseline [m]	Temporal separation [days]
19920901-19920728	-420	-35
19930713-19920728	386	-350
19930921-19920901	-337	-385
19950601-19920728	-145	-1038
19950602-19920728	-119	-1039
19950602-19950601	31	-1
19950706-19920728	91	-1073
19950706-19930713	-346	-723
19950706-19950601	181	-35

19950706-19950602	150	-34
19950707-19920728	89	-1074
19950707-19930713	-341	-724
19950707-19950601	184	-36
19950707-19950602	153	-35
19950707-19950706	6	-1
19950914-19920728	100	-1143
19950914-19930713	-310	-793
19950914-19950601	213	-105
19950914-19950602	182	-104
19950914-19950706	37	-70
19950914-19950707	31	-69
19950915-19920728	69	-1144
19950915-19920901	432	-1109
19950915-19930713	-370	-794
19950915-19950601	153	-106
19950915-19950602	122	-105
19950915-19950706	-29	-71
19950915-19950707	-31	-70
19950915-19950914	-59	-1
19951019-19920901	-333	-1143
19951019-19930921	24	-758
19951020-19920901	-395	-1144
19951020-19930921	-66	-759
19951020-19951019	-62	-1
19970606-19950601	44	-736
19970606-19950602	13	-735

19970606-19950706	-137	-701
19970606-19950707	-141	-700
19970606-19950914	-170	-631
19970606-19950915	-111	-630
19970815-19920901	-65	-1809
19970815-19930921	280	-1424
19970815-19951019	279	-666
19970815-19951020	341	-665
19970919-19930713	-278	-1529
19970919-19950601	243	-841
19970919-19950602	213	-840
19970919-19950706	74	-806
19970919-19950707	68	-805
19970919-19950914	37	-736
19970919-19950915	93	-735
19990924-19950601	-51	-1576
19990924-19950602	-78	-1575
19990924-19950706	-222	-1541
19990924-19950707	-224	-1540
19990924-19950914	-251	-1471
19990924-19950915	-193	-1470
19990924-19970815	315	-770
19990924-19970919	-277	-735

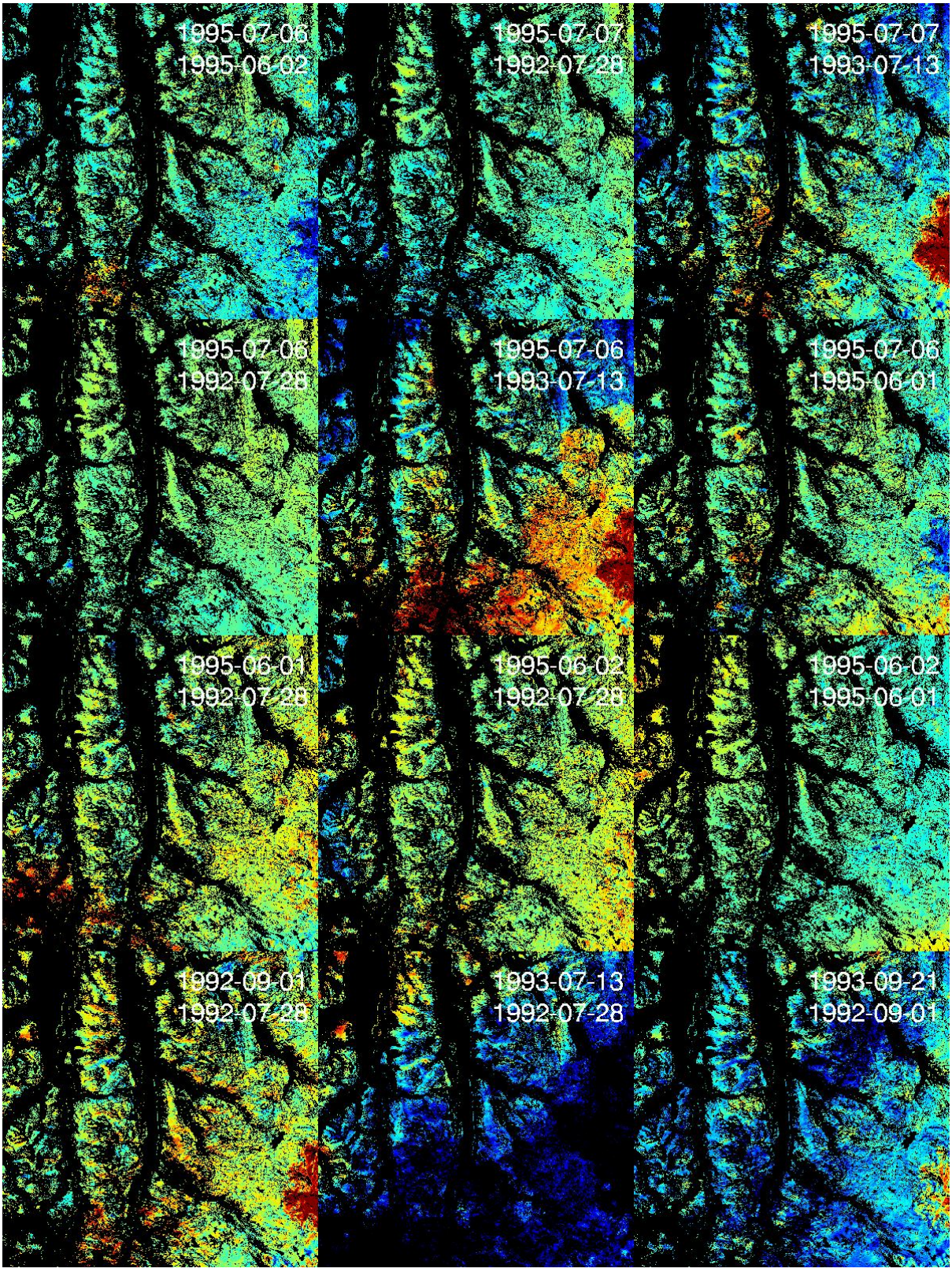
1995-07-06
1995-06-02
1995-07-07
1992-07-28
1995-07-07
1993-07-13
1995-07-06
1992-07-28
1995-07-06
1993-07-13
1995-07-06
1995-06-01
1995-06-01
1992-07-28
1995-06-02
1992-07-28
1995-06-02
1995-06-01
1992-09-01
1992-07-28
1993-07-13
1992-07-28
1993-09-21
1992-09-01

Figure DR2

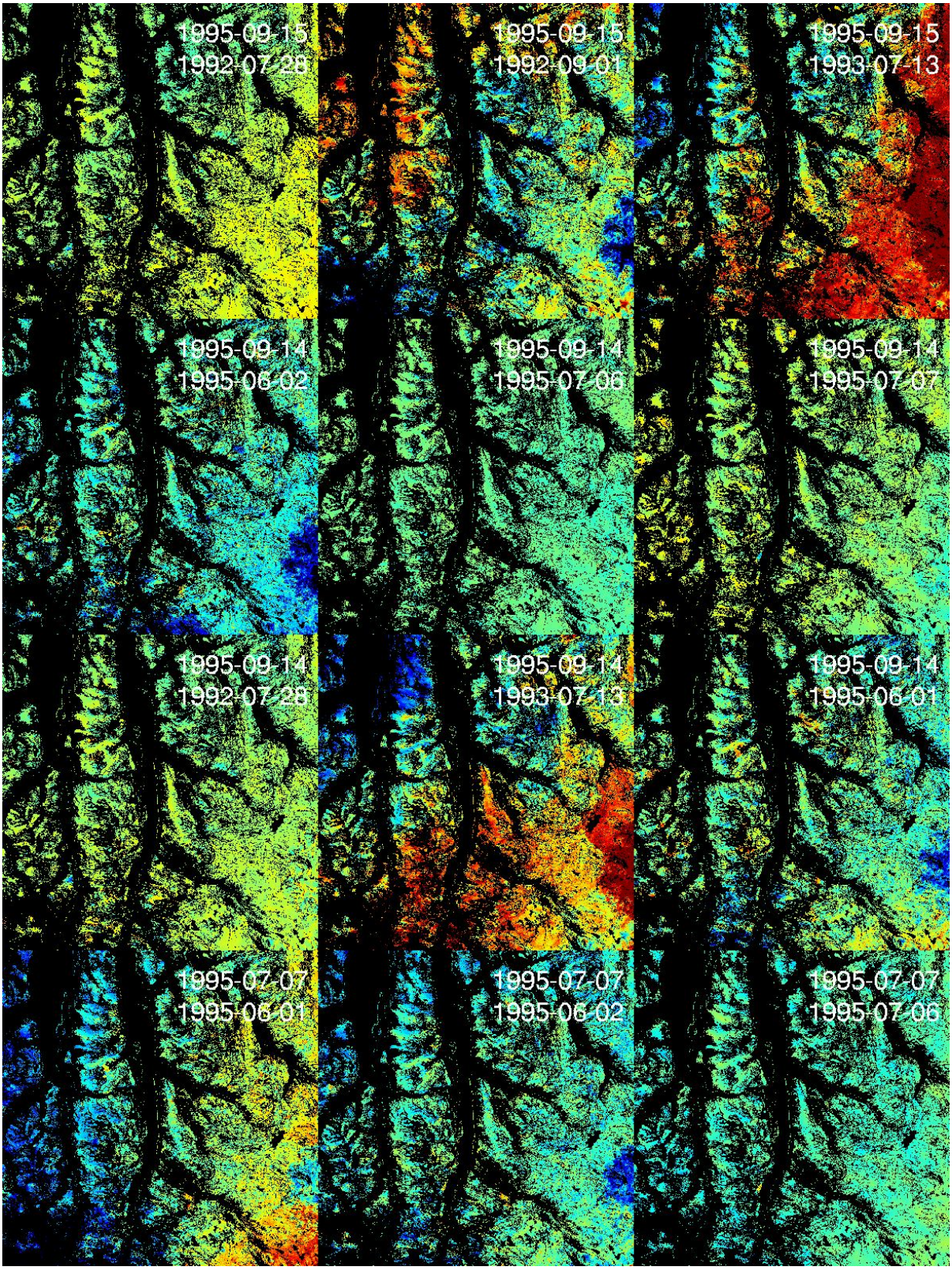
1995-09-15
1992-07-28
1995-09-15
1992-09-01
1995-09-15
1993-07-13
1995-09-14
1995-06-02
1995-09-14
1995-07-06
1995-09-14
1995-07-07
1995-09-14
1992-07-28
1995-09-14
1993-07-13
1995-09-14
1995-06-01
1995-07-07
1995-06-01
1995-07-07
1995-06-02
1995-07-07
1995-07-06

Figure DR3

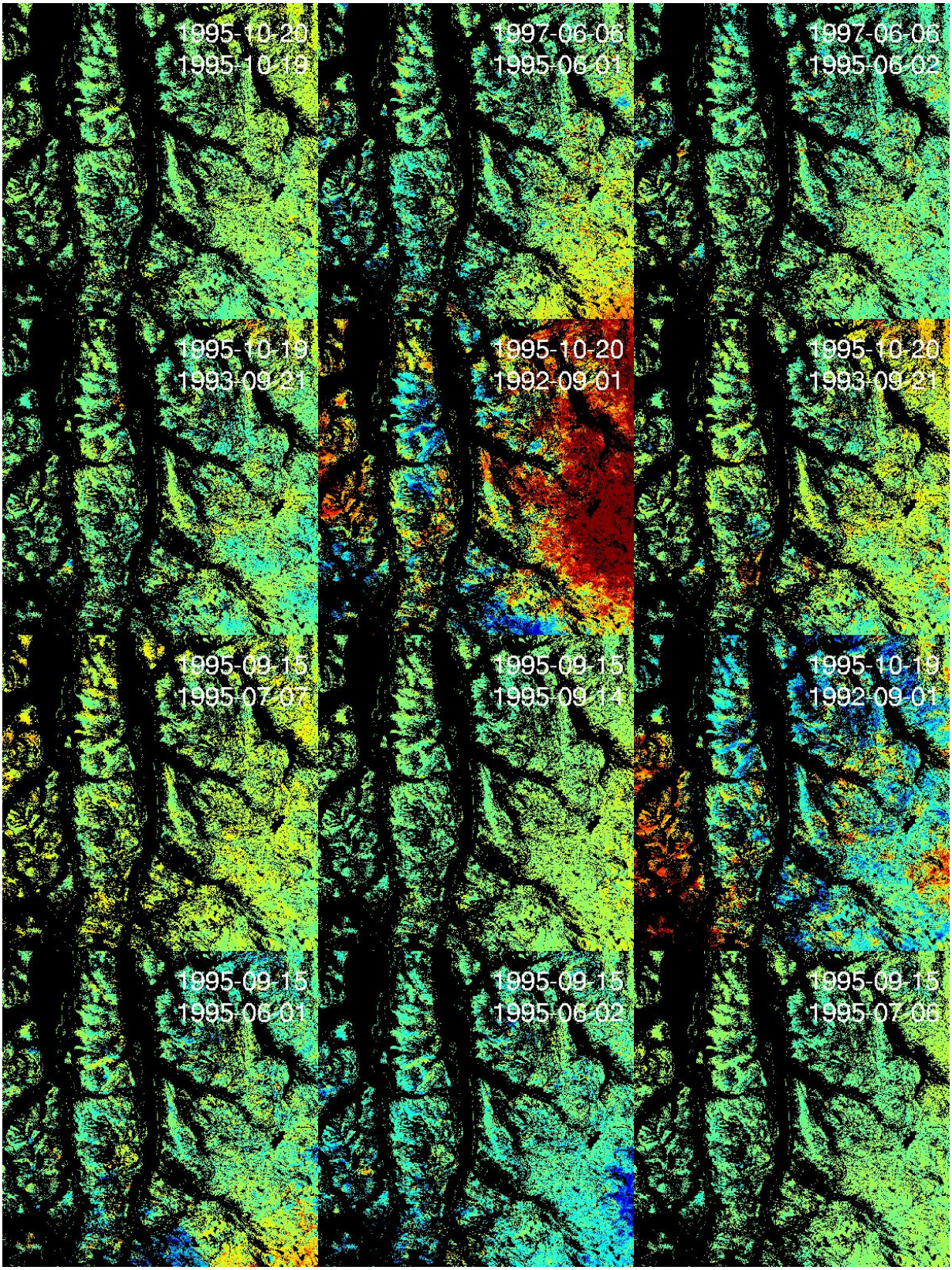
1995-10-20
1995-10-19
1997-06-06
1995-06-01
1997-06-06
1995-06-02
1995-10-19
1993-09-21
1995-10-20
1992-09-01
1995-10-20
1993-09-21
1995-09-15
1995-07-07
1995-09-15
1995-09-14
1995-10-19
1992-09-01
1995-09-15
1995-06-01
1995-09-15
1995-06-02
1995-09-15
1995-07-06

Figure DR4

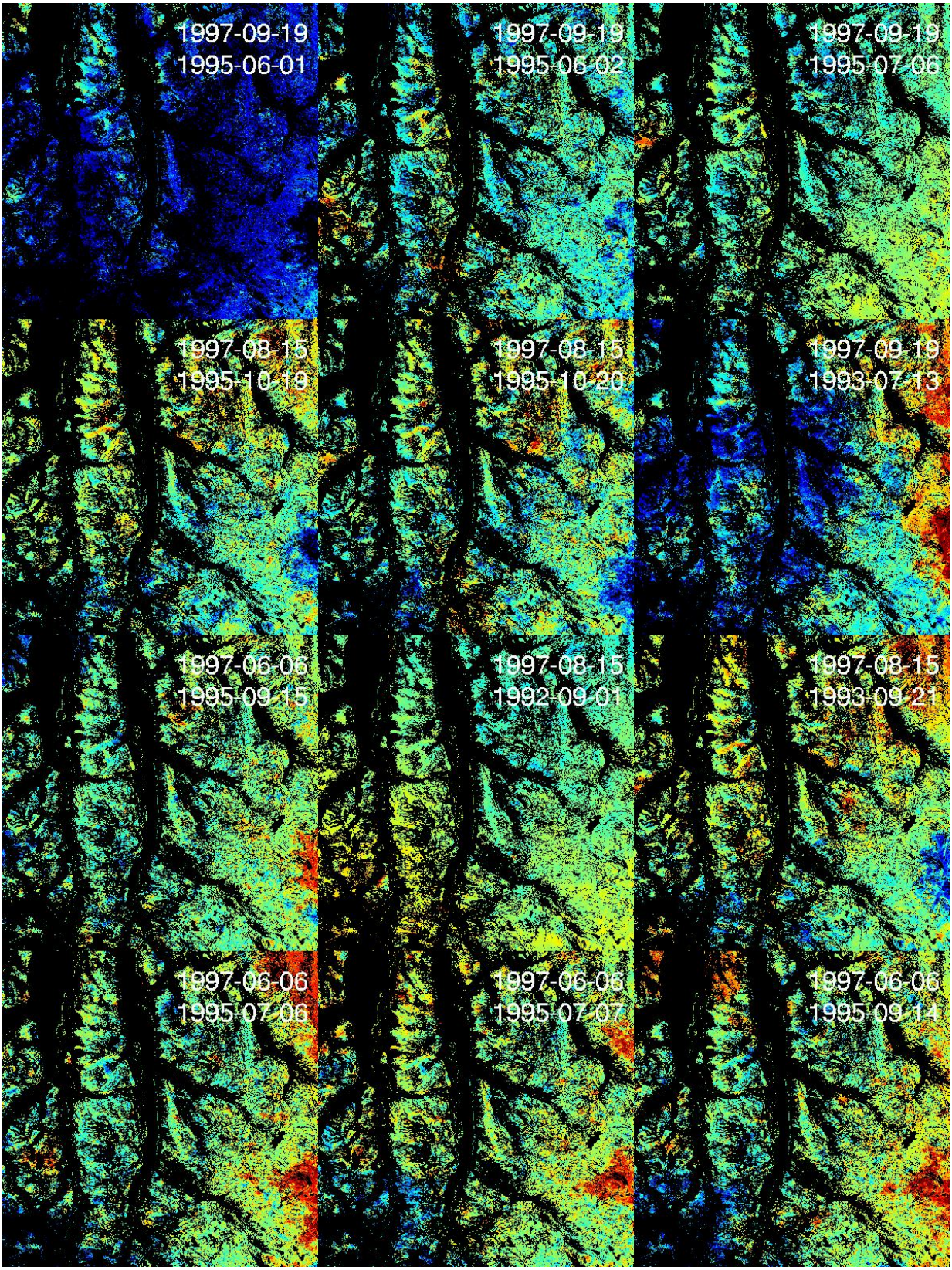
1997-09-19
1995-06-01
1997-09-19
1995-06-02
1997-09-19
1995-07-06
1997-08-15
1995-10-19
1997-08-15
1995-10-20
1997-09-19
1993-07-13
1997-06-06
1995-09-15
1997-08-15
1992-09-01
1997-08-15
1993-09-21
1997-06-06
1995-07-06
1997-06-06
1995-07-07
1997-06-06
1995-09-14

Figure DR5

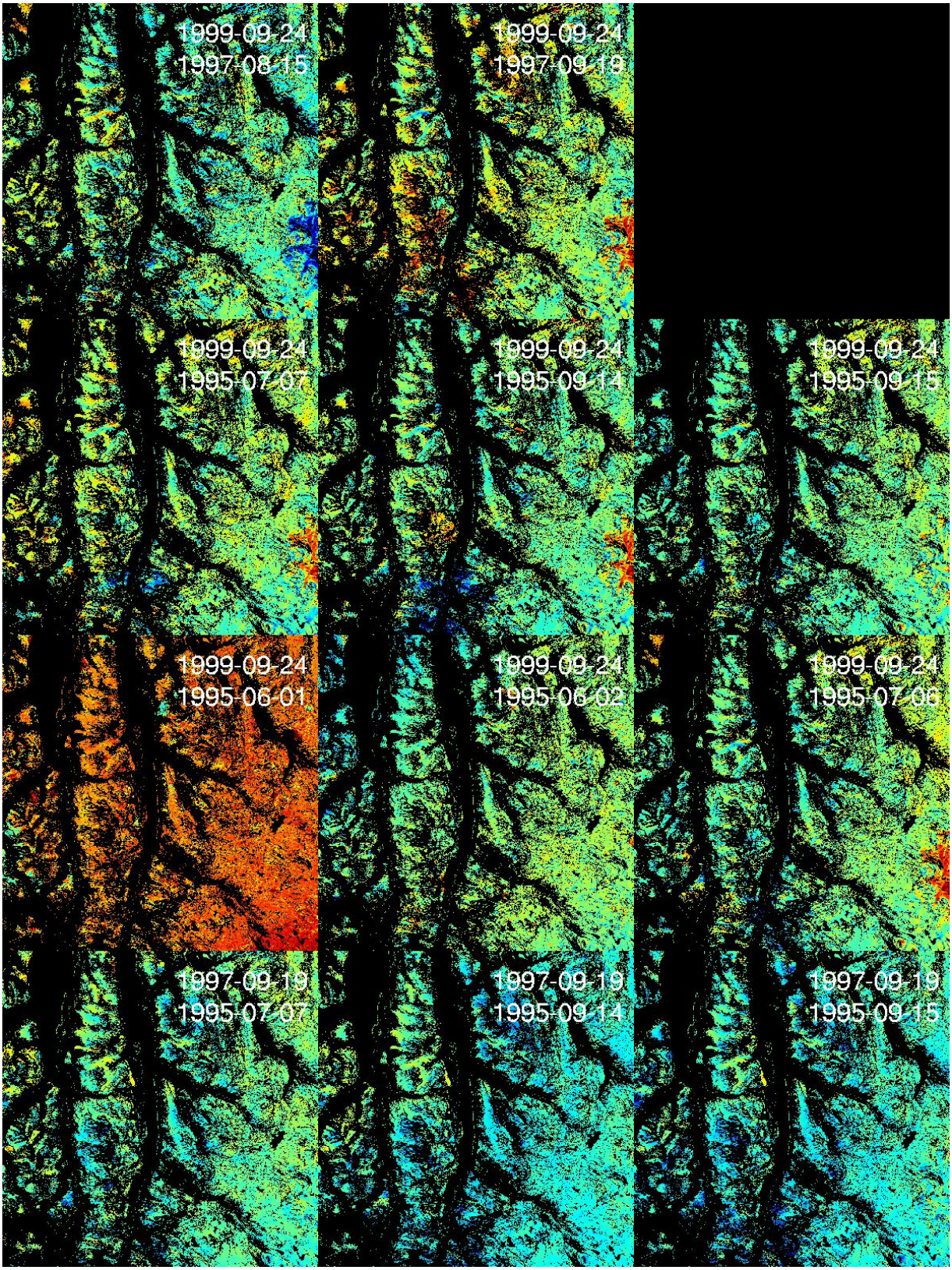
1999-09-24
1997-08-15
1999-09-24
1997-09-19
1999-09-24
1995-07-07
1999-09-24
1995-09-14
1999-09-24
1995-09-15
1999-09-24
1995-06-01
1999-09-24
1995-06-02
1999-09-24
1995-07-06
1997-09-19
1995-07-07
1997-09-19
1995-09-14
1997-09-19
1995-09-15

Figure DR6

Figures DR2-DR6: Unwrapped interferograms. The phase values have been scaled between (-4π, 4π) in order to illustrate possible phase unwrapping errors. See Table 1 for details about the interferometric baselines. The unwrapped interferograms still include possible heterogenous atmospheric artifacts and residual phase due to errors in the digital elevation model.

DR item 3: Complete INSAR profile data

The INSAR data described in the main text and in the Supplement text above were archived as a Band Interleaved file in UTM33N coordinates in ERMapper .ers format. A small counterclockwise rotation was applied to align the edges of the non-null data with a NS azimuth. A filter was applied to remove fast motion representing actual landslides (see text). The grid was then sliced into twenty-three EW bands of approximately 500 meters width (20 pixels). A random subset of these pixels was then plotted against native Easting coordinates. The complete set of EW cross sections (Figures DR8-DR30) are presented below, keyed to a location map (Figure DR7).

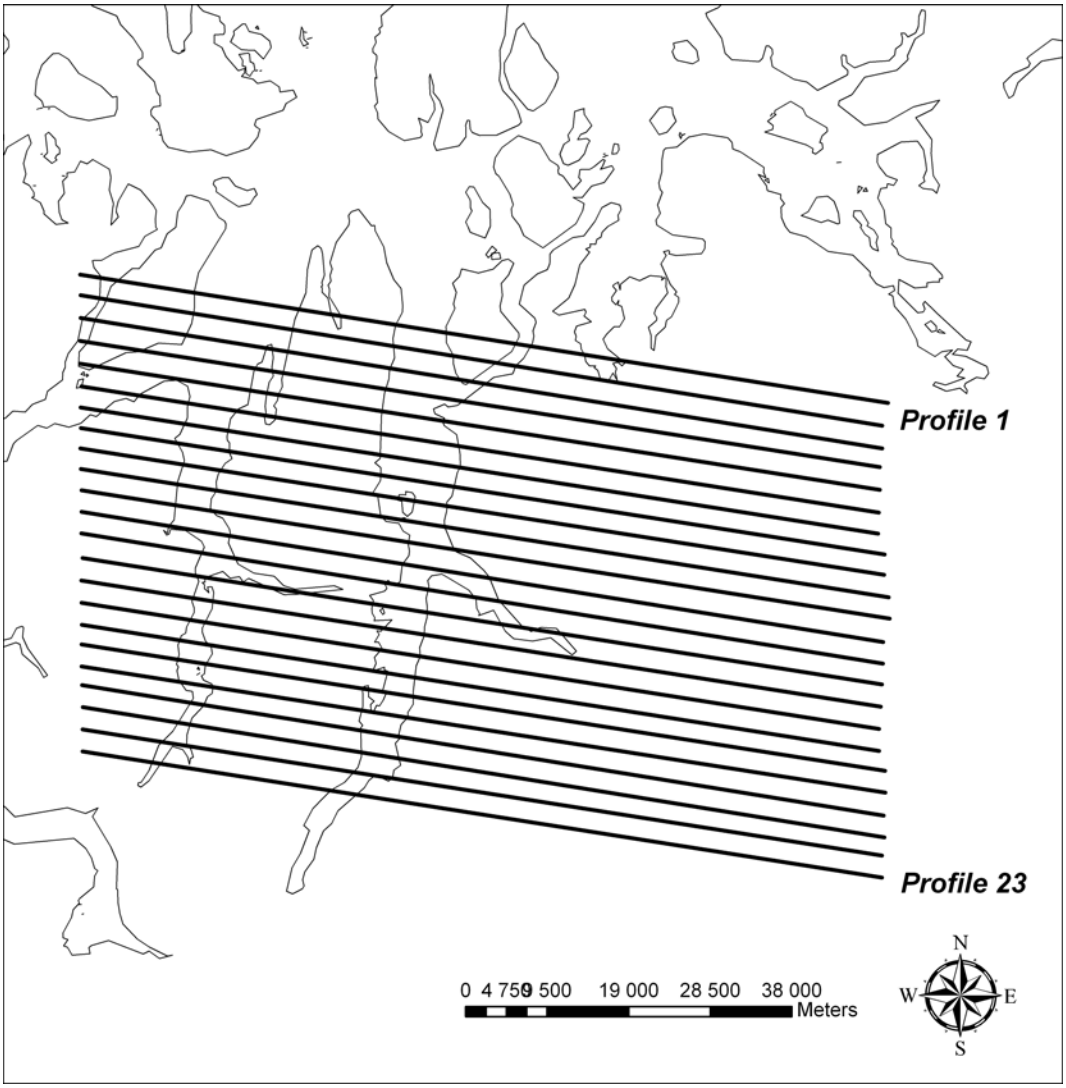

Figure DR7

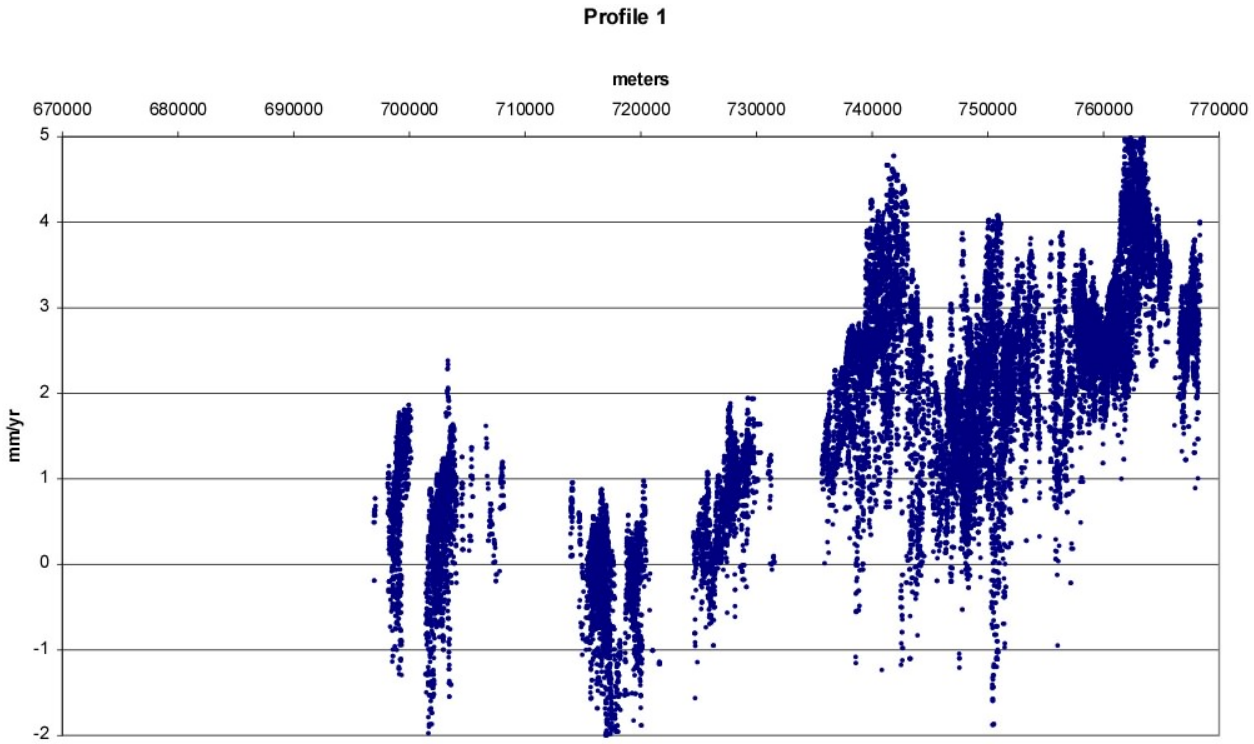

Figure DR8: Profile 1

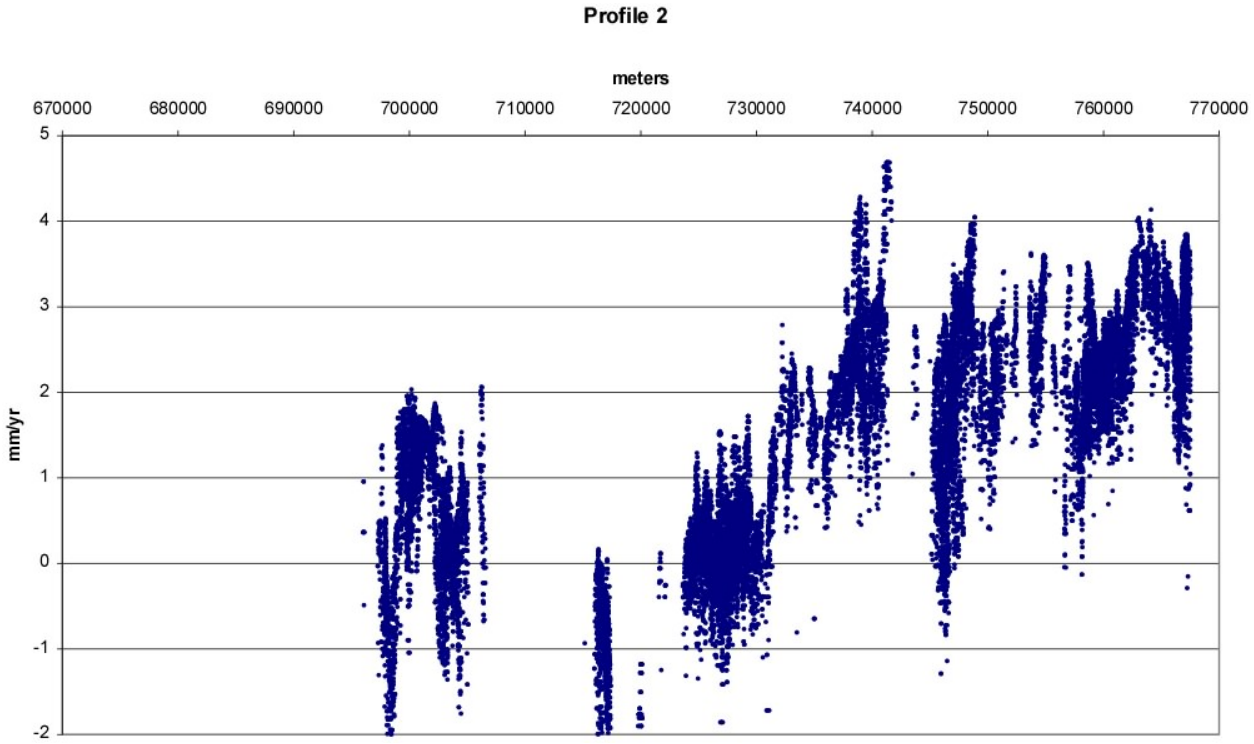

Figure DR9: Profile 2

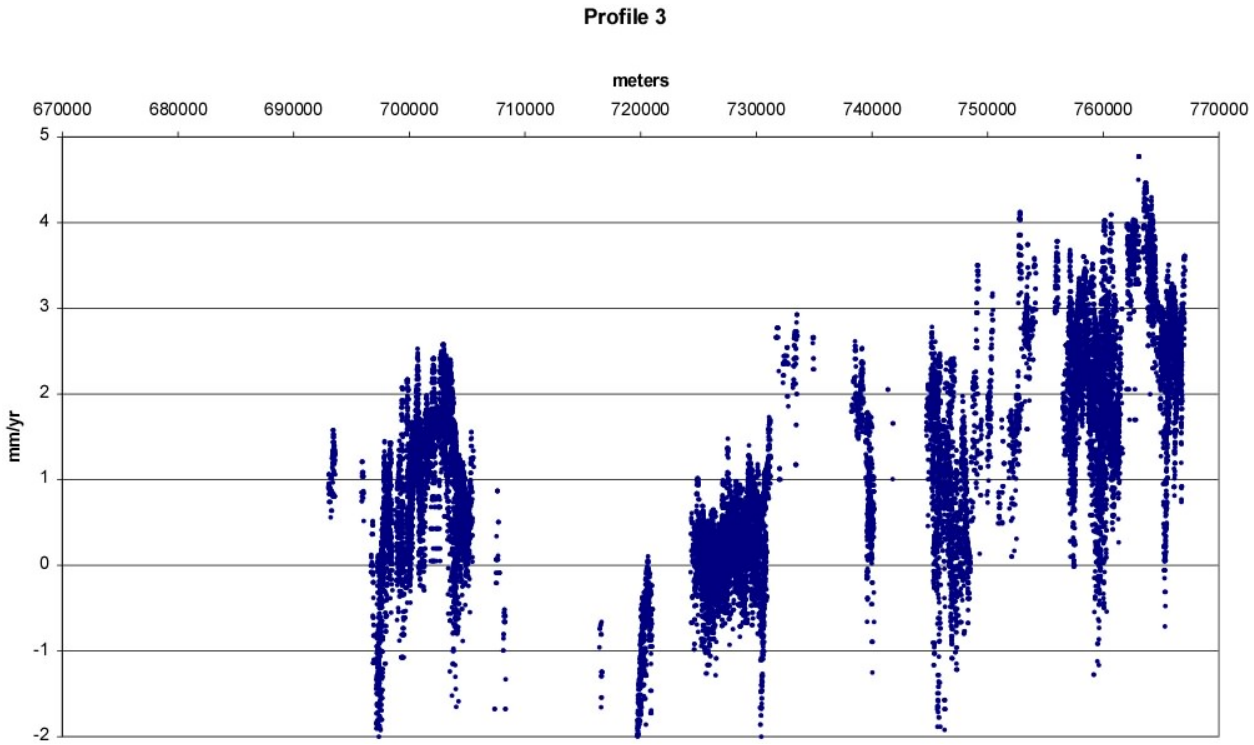

Figure DR10: Profile 3

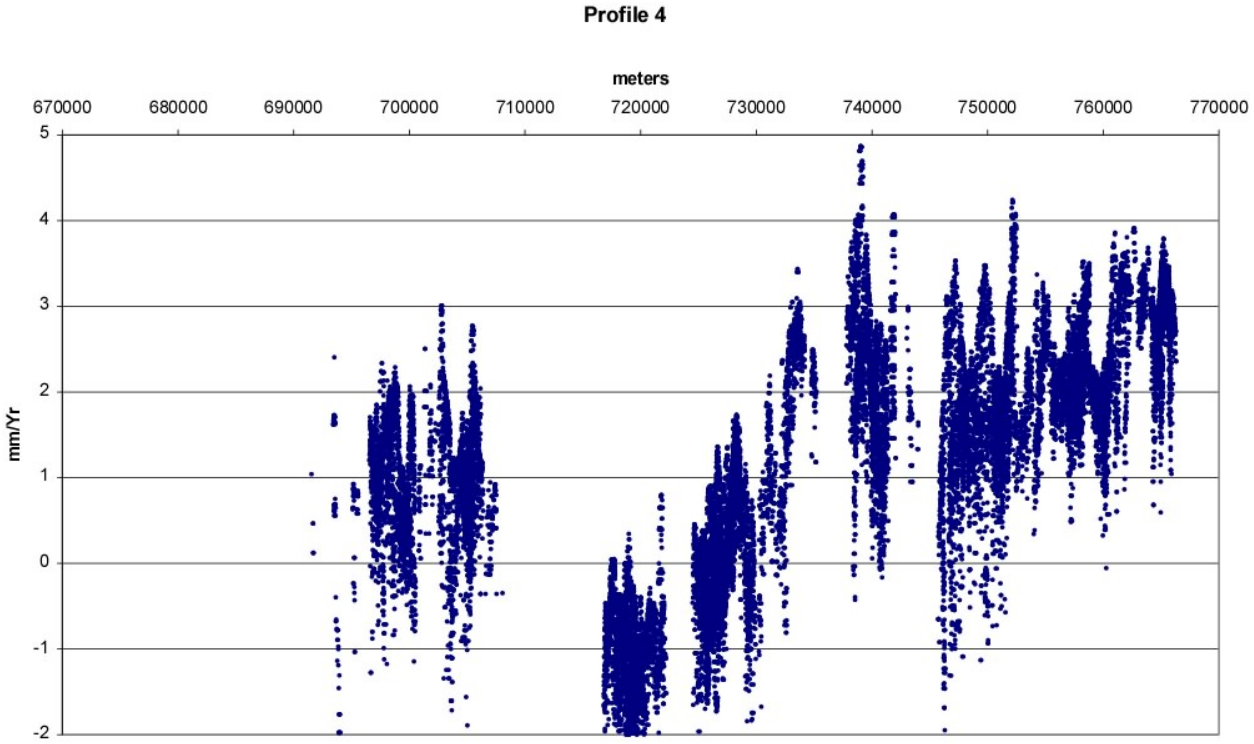

Figure DR11: Profile 4

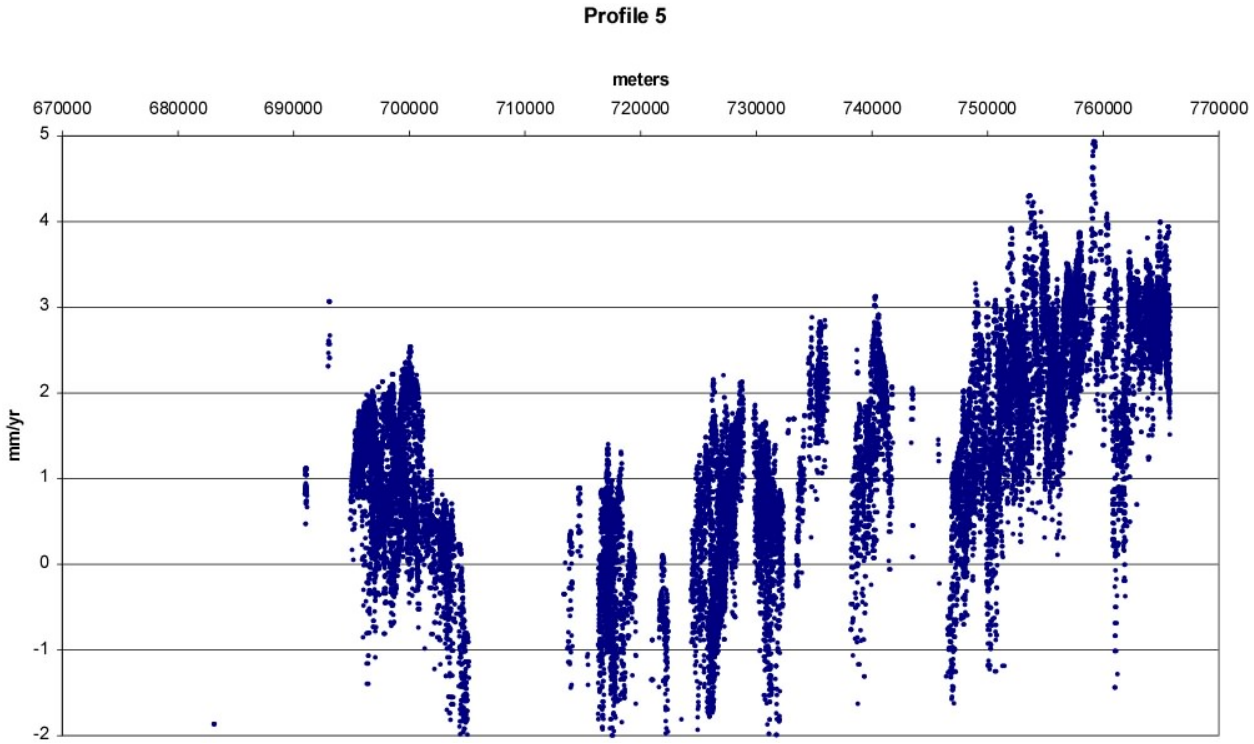

Figure DR12: Profile 5

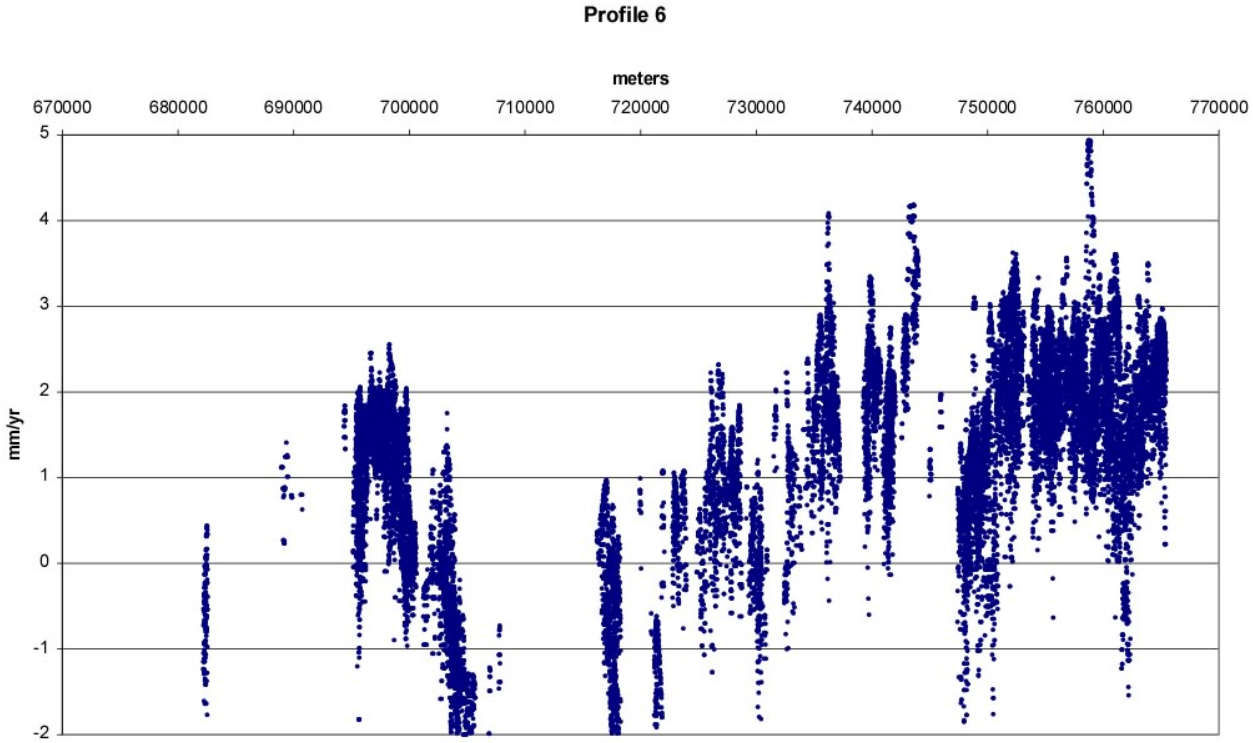

Figure DR13: Profile 6

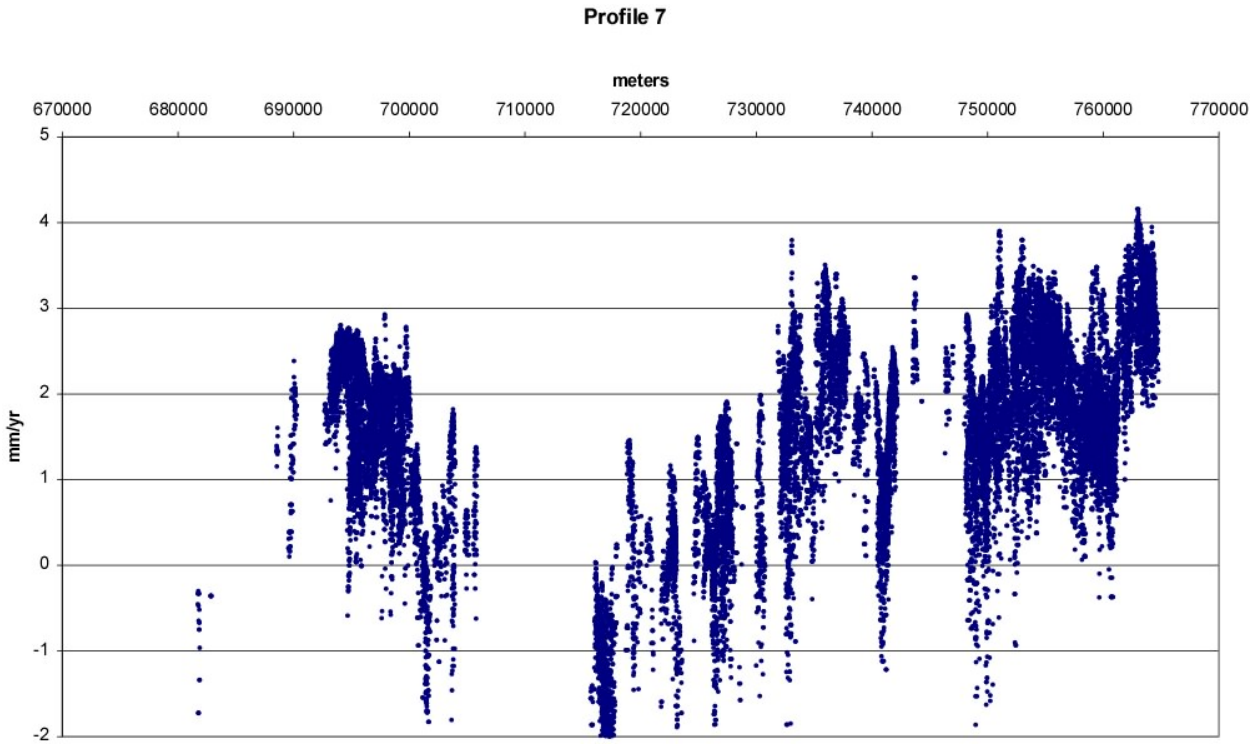

Figure DR14: Profile 7

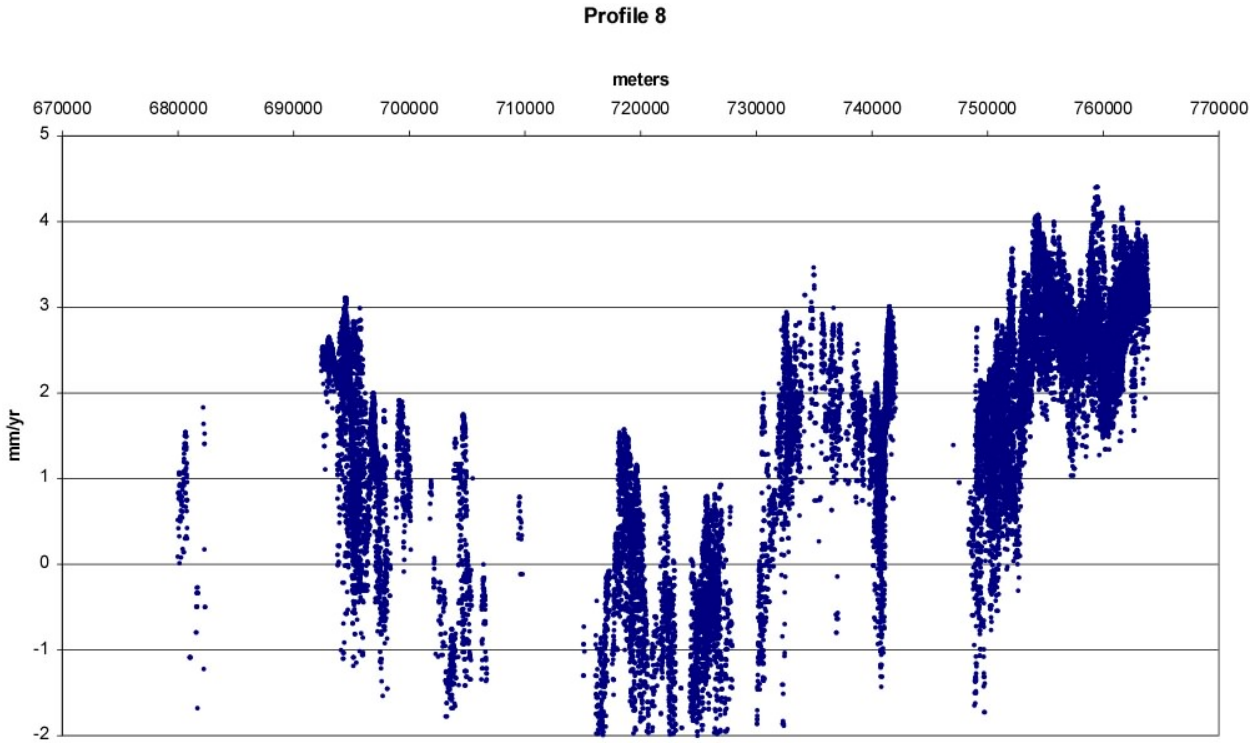

Figure DR15: Profile 8

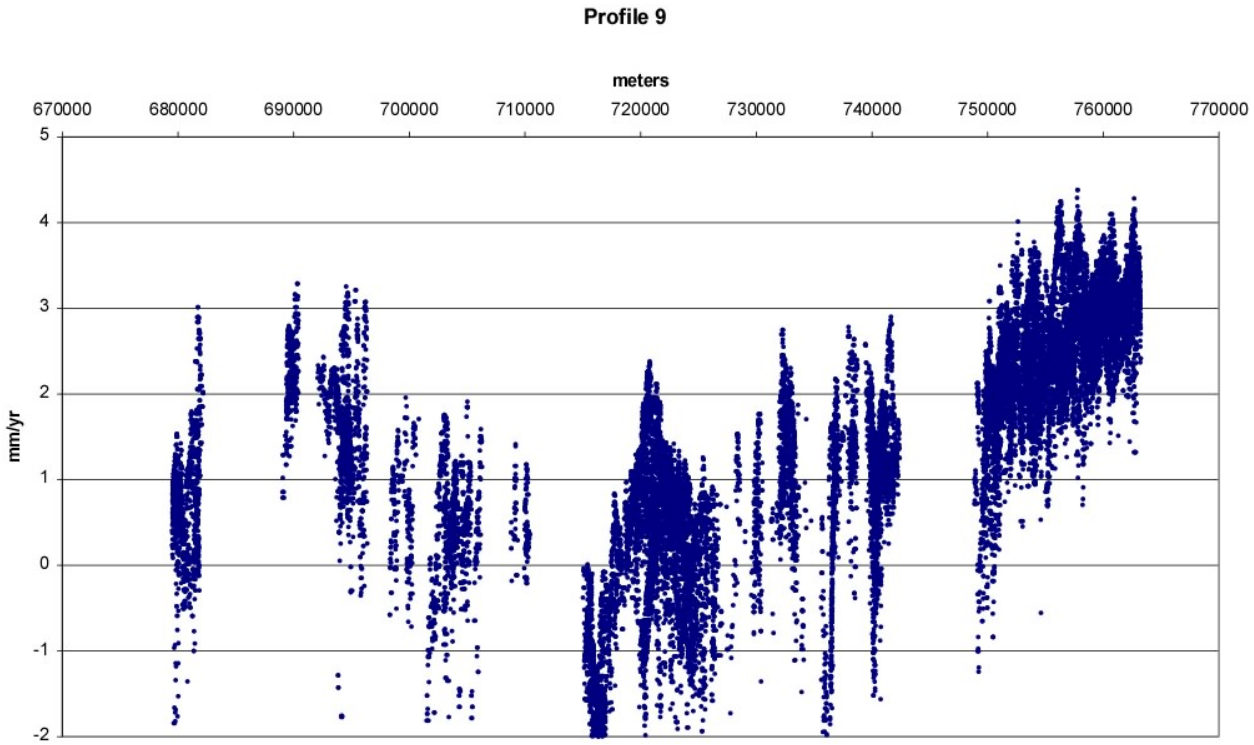

Figure DR16: Profile 9

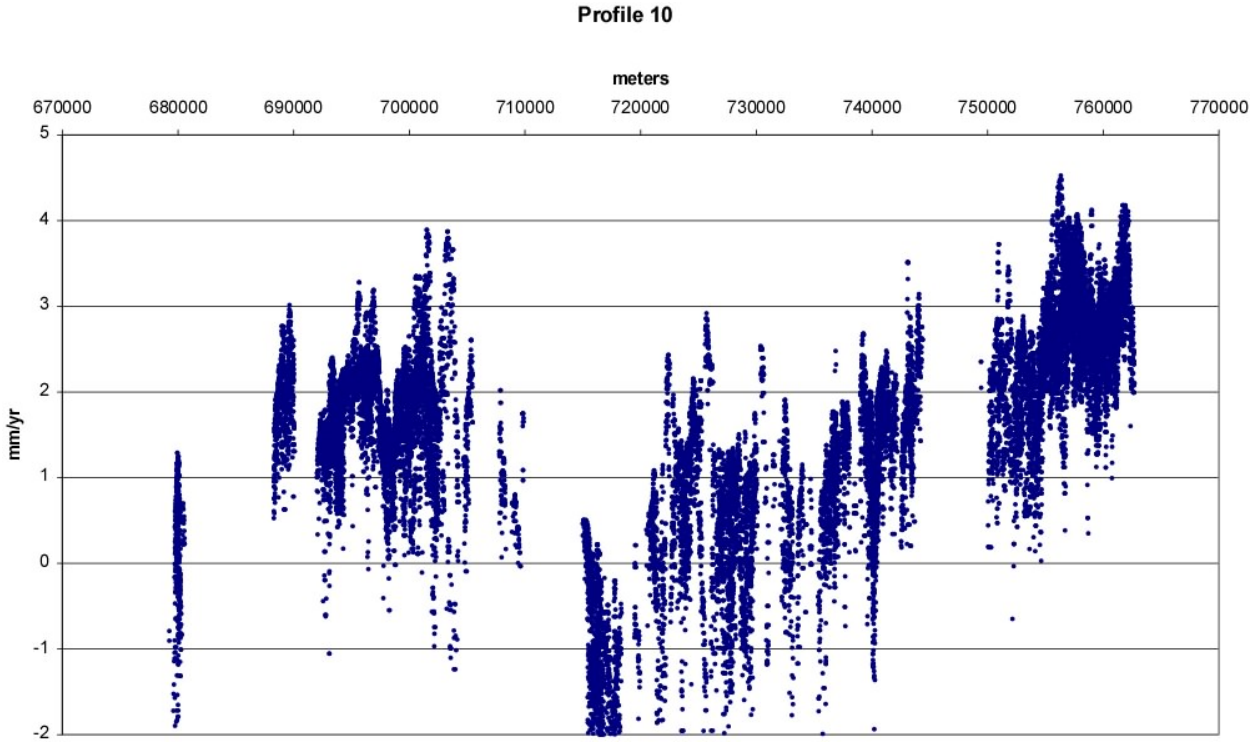

Figure DR17: Profile 10

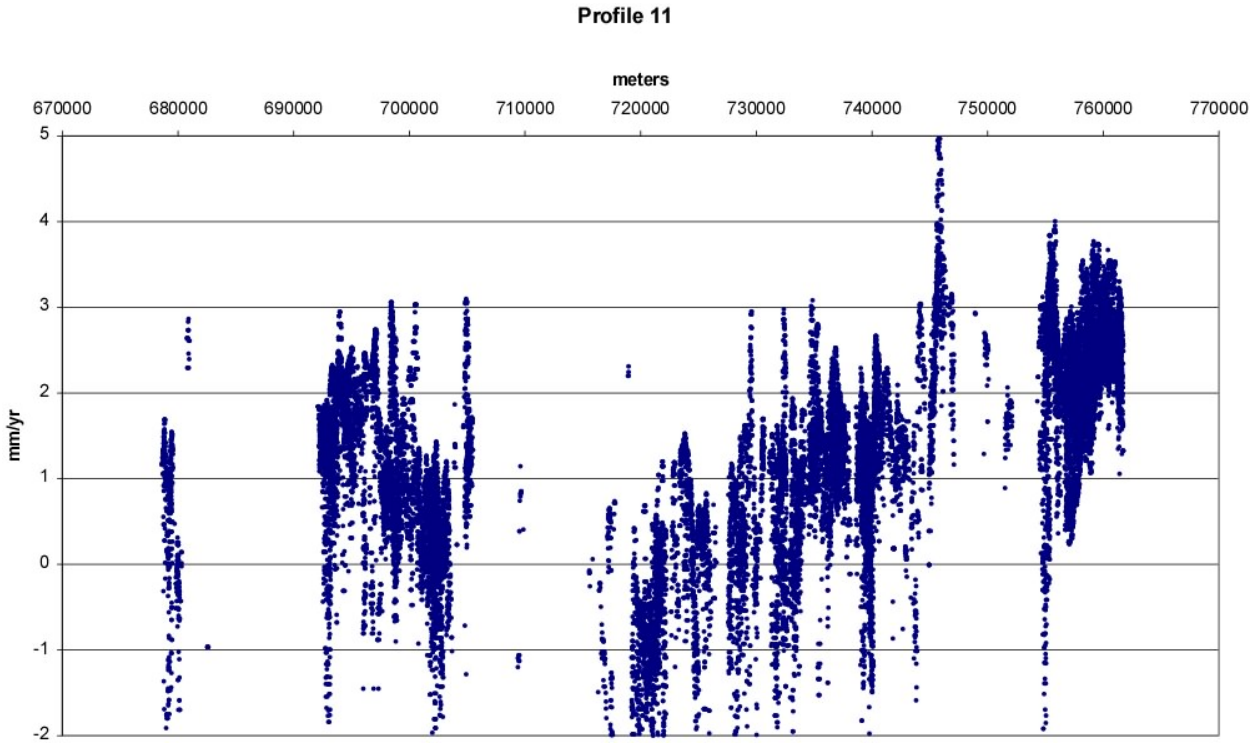

Figure DR18: Profile 11

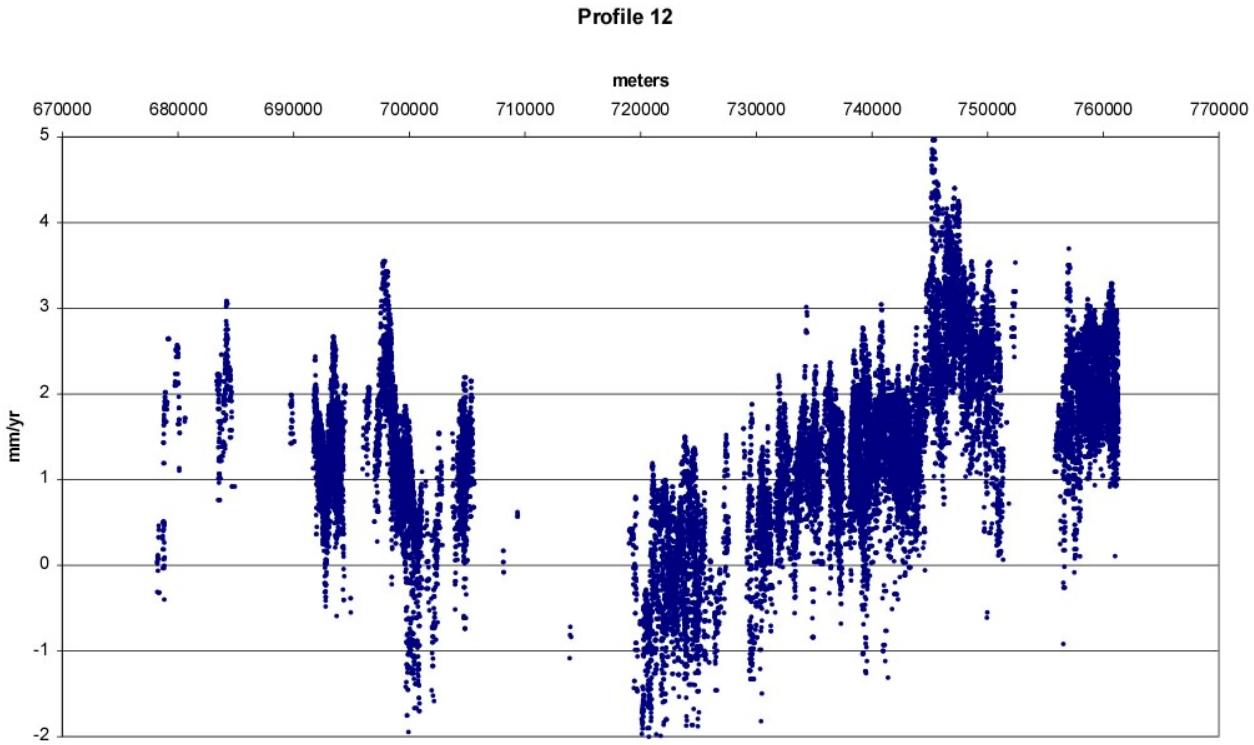

Figure DR19: Profile 12

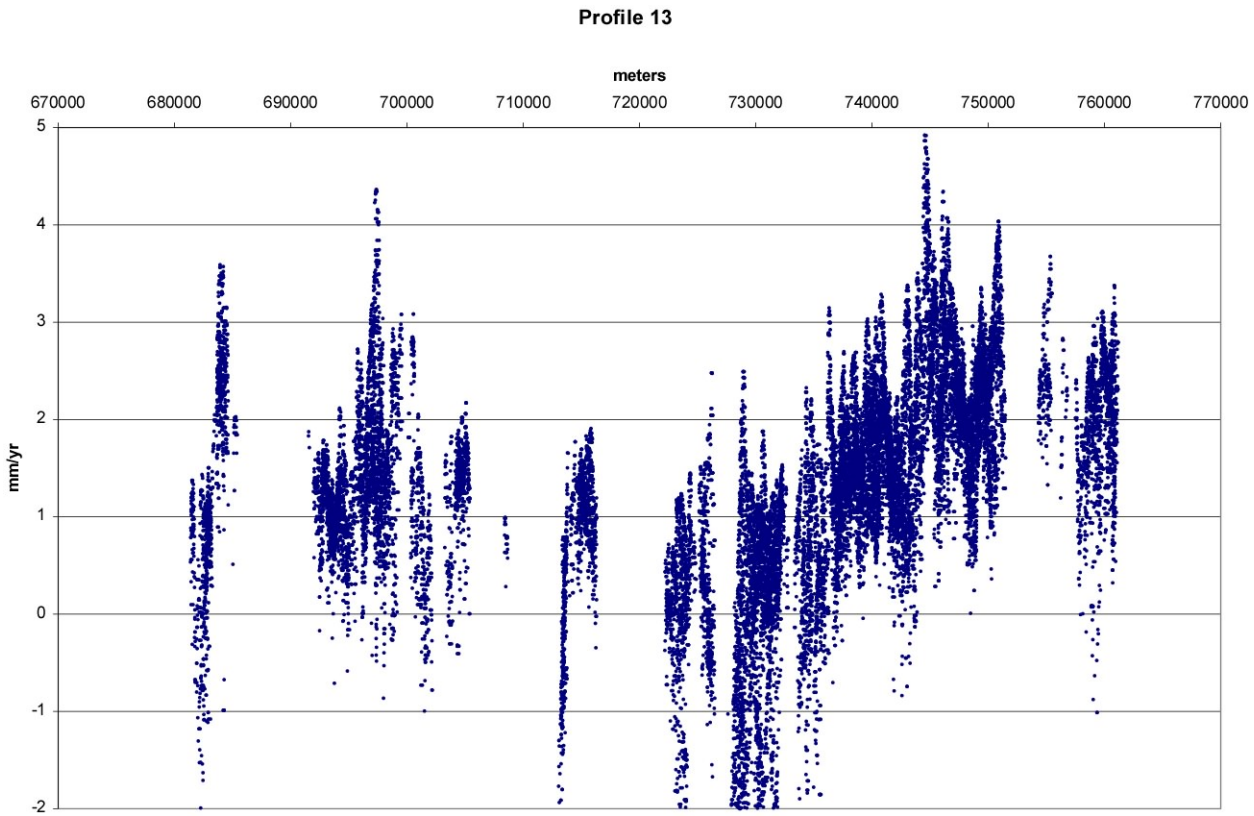

Figure DR20: Profile 13

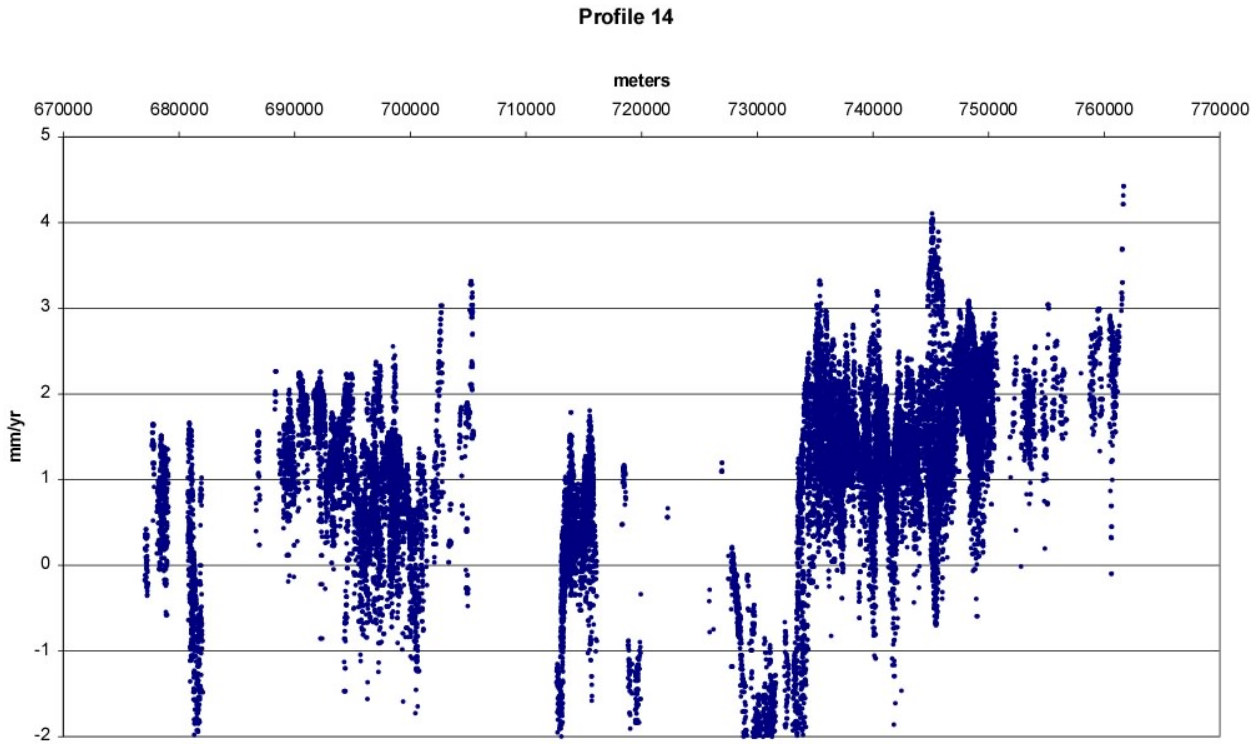

Figure DR21: Profile 14

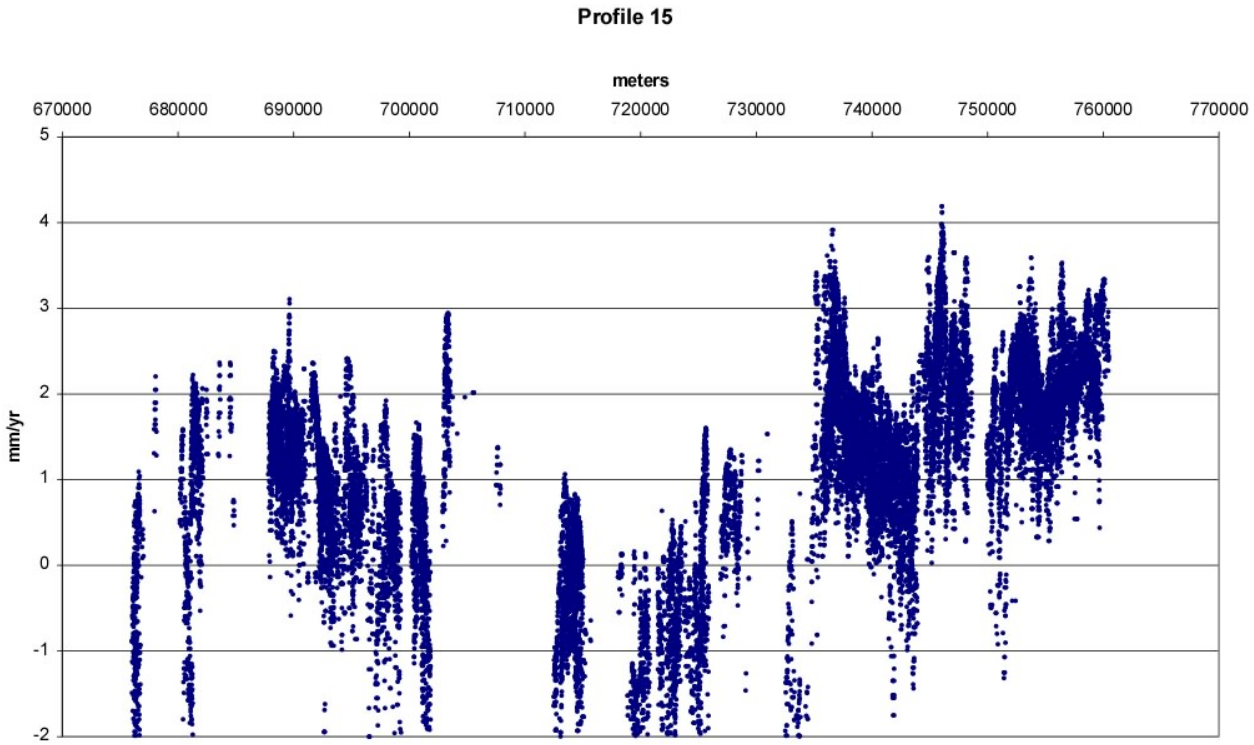

Figure DR22: Profile 15

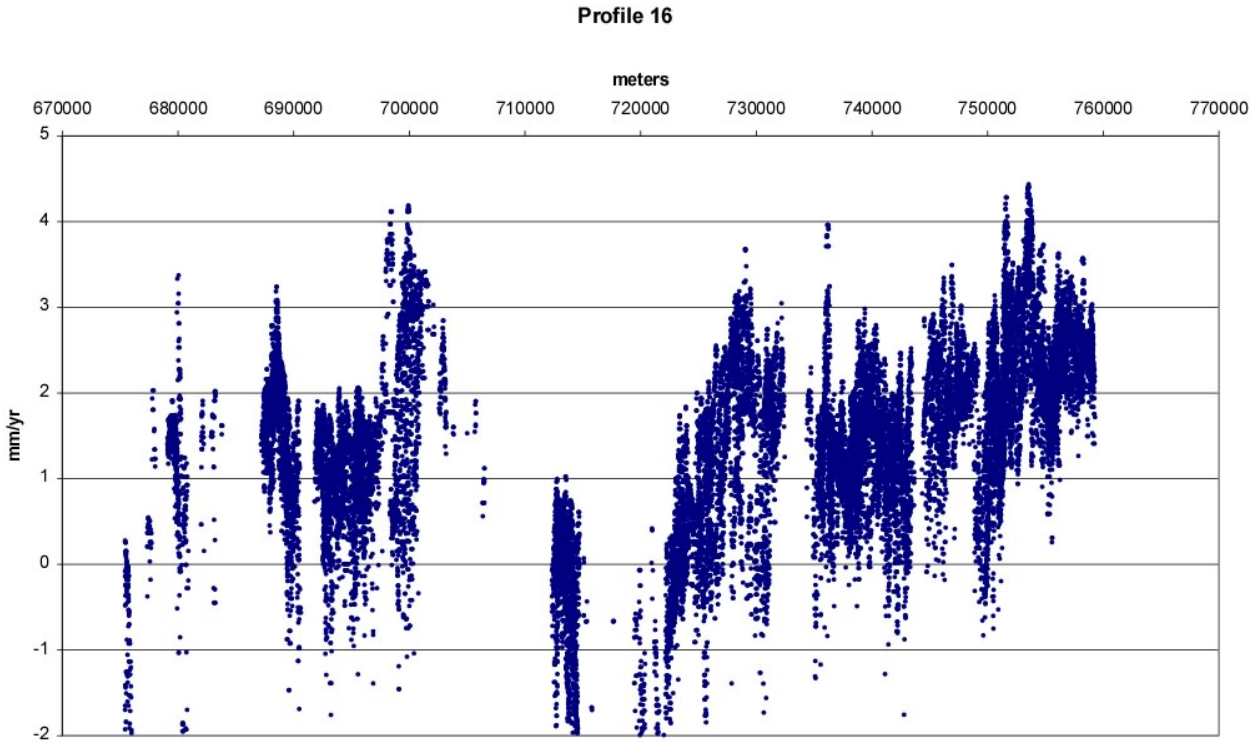

Figure DR23: Profile 16

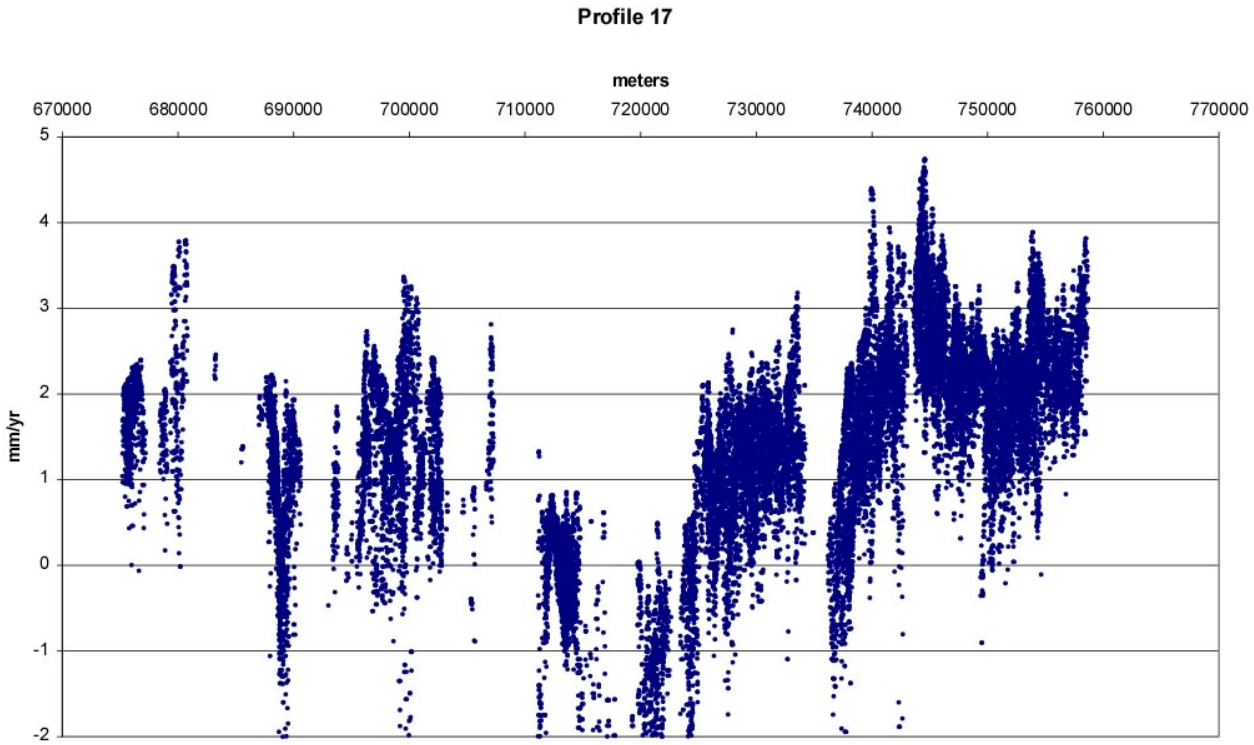

Figure DR24: Profile 17

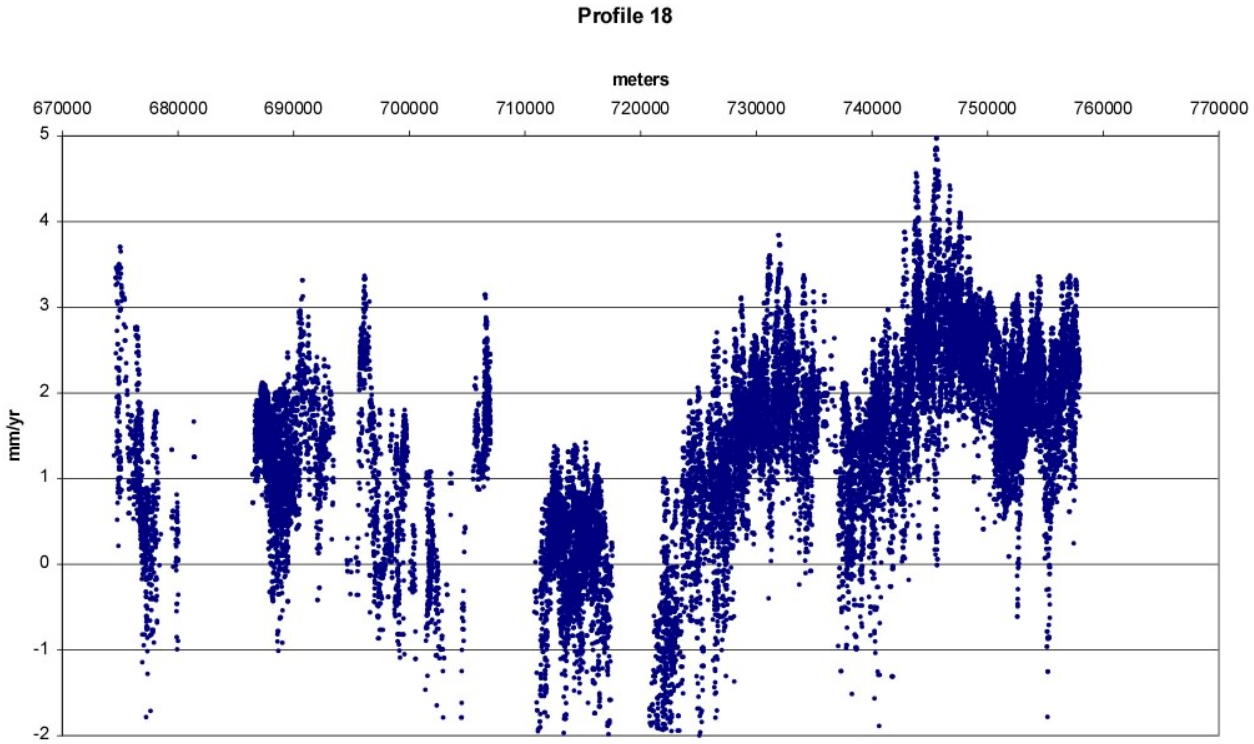

Figure DR25: Profile 18

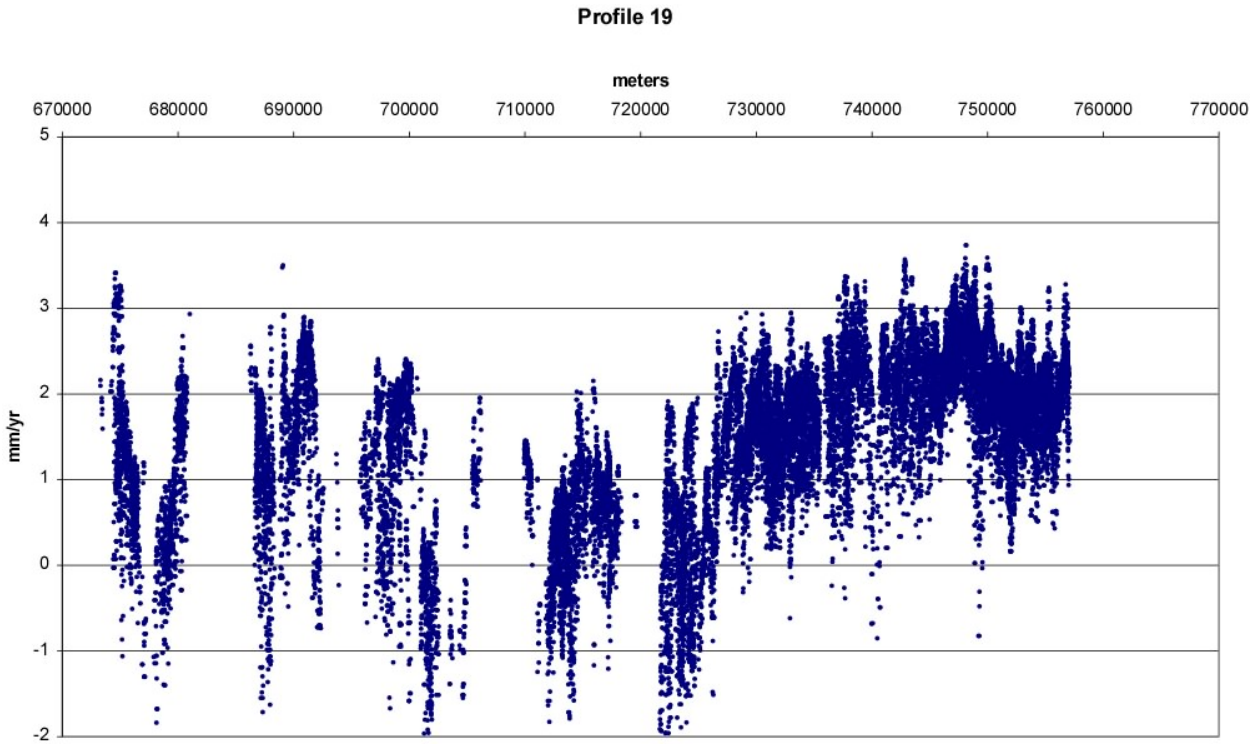

Figure DR26: Profile 19

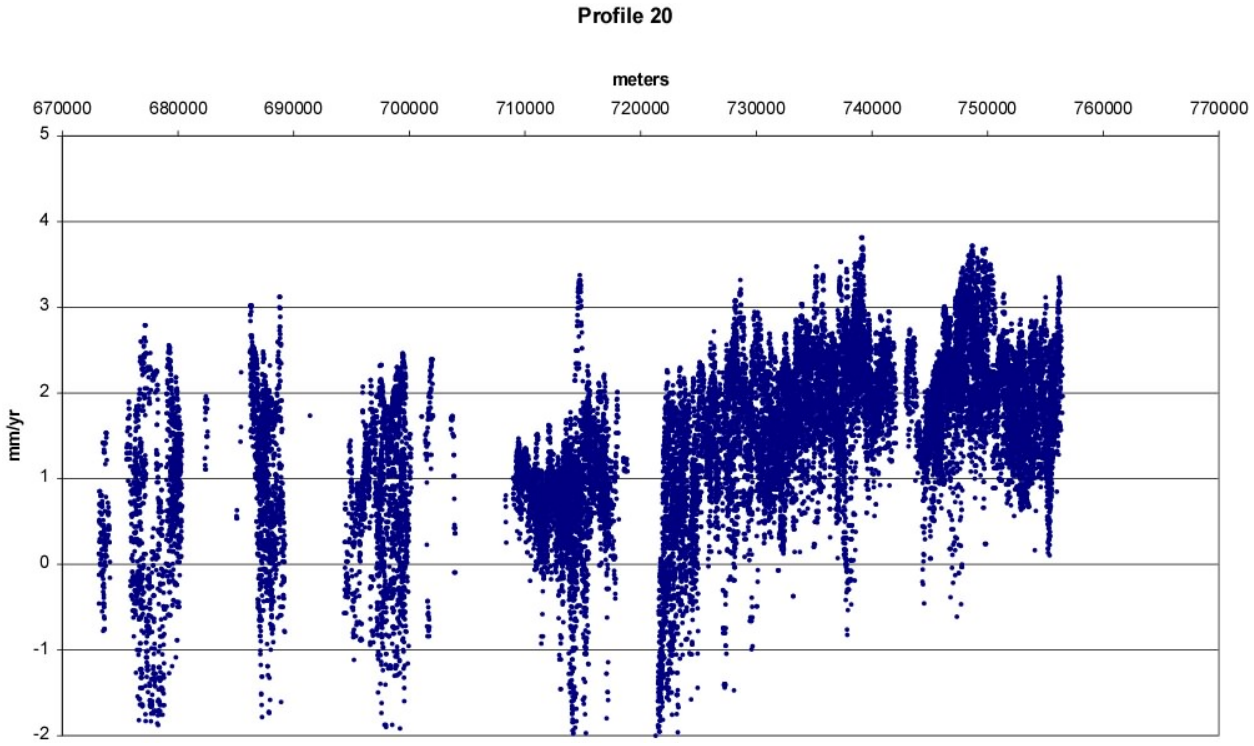

Figure DR27: Profile 20

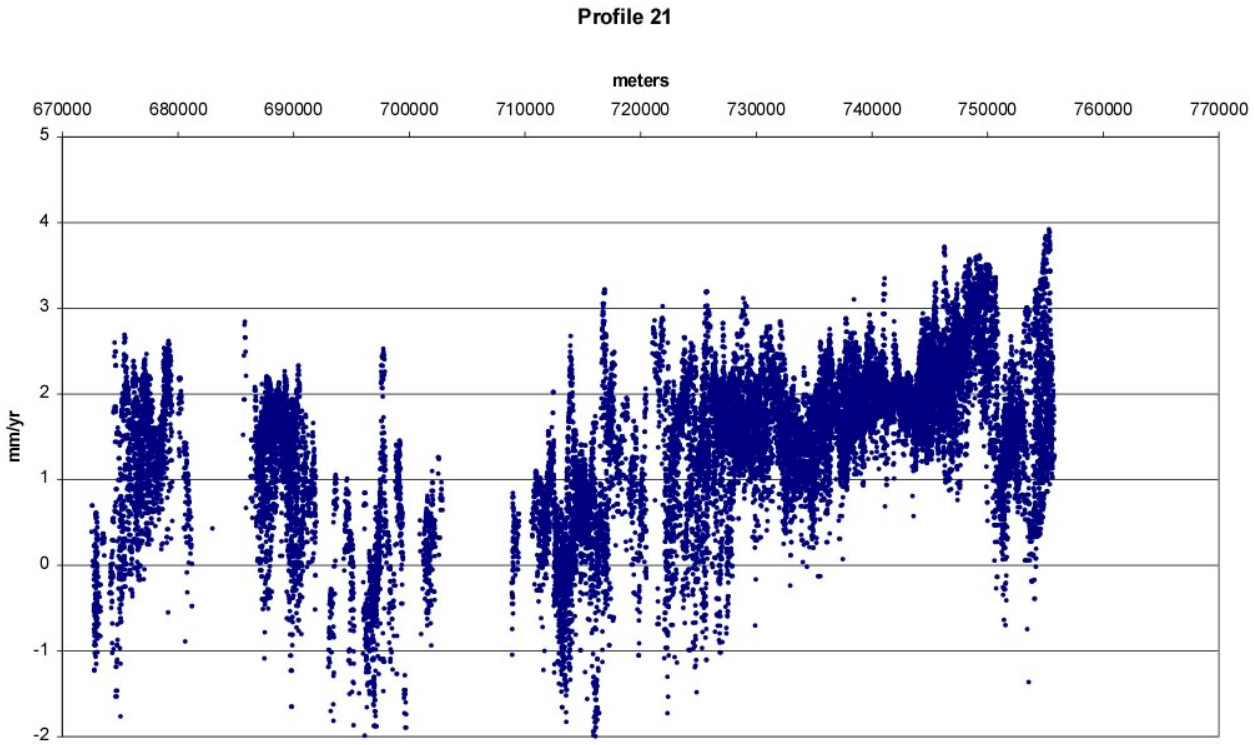

Figure DR28: Profile 21

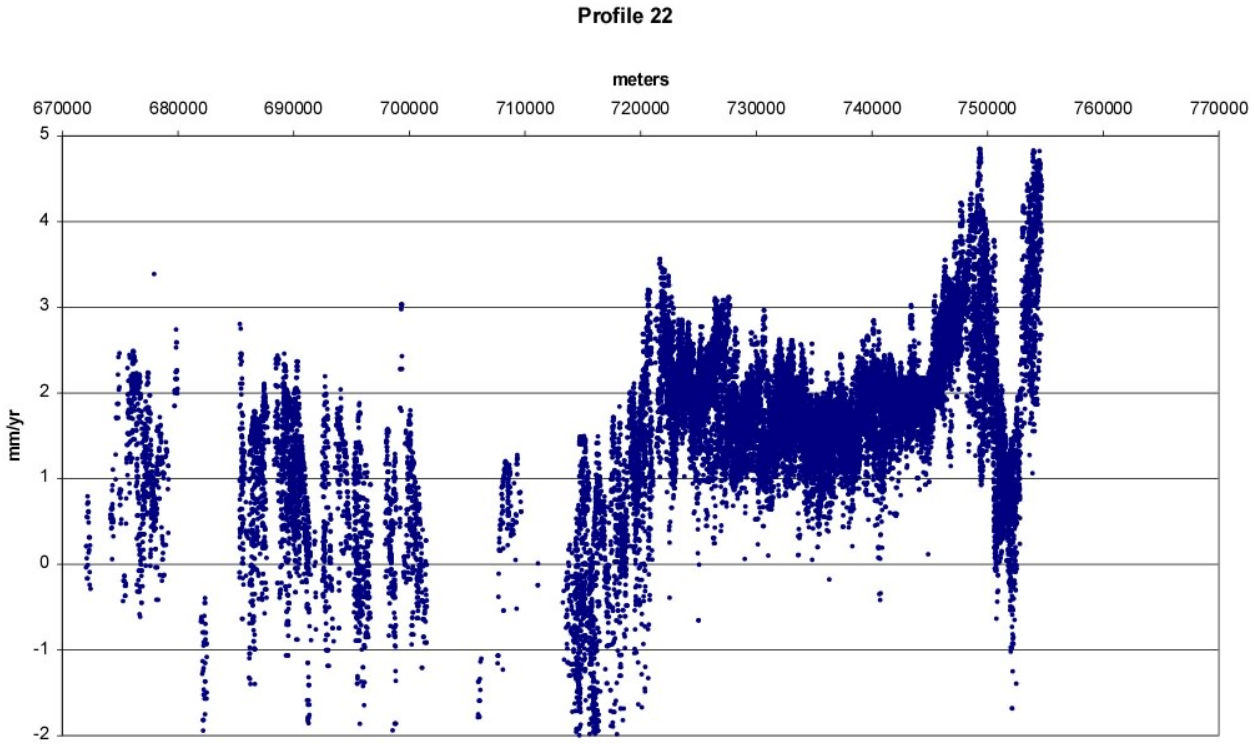

Figure DR29: Profile 22

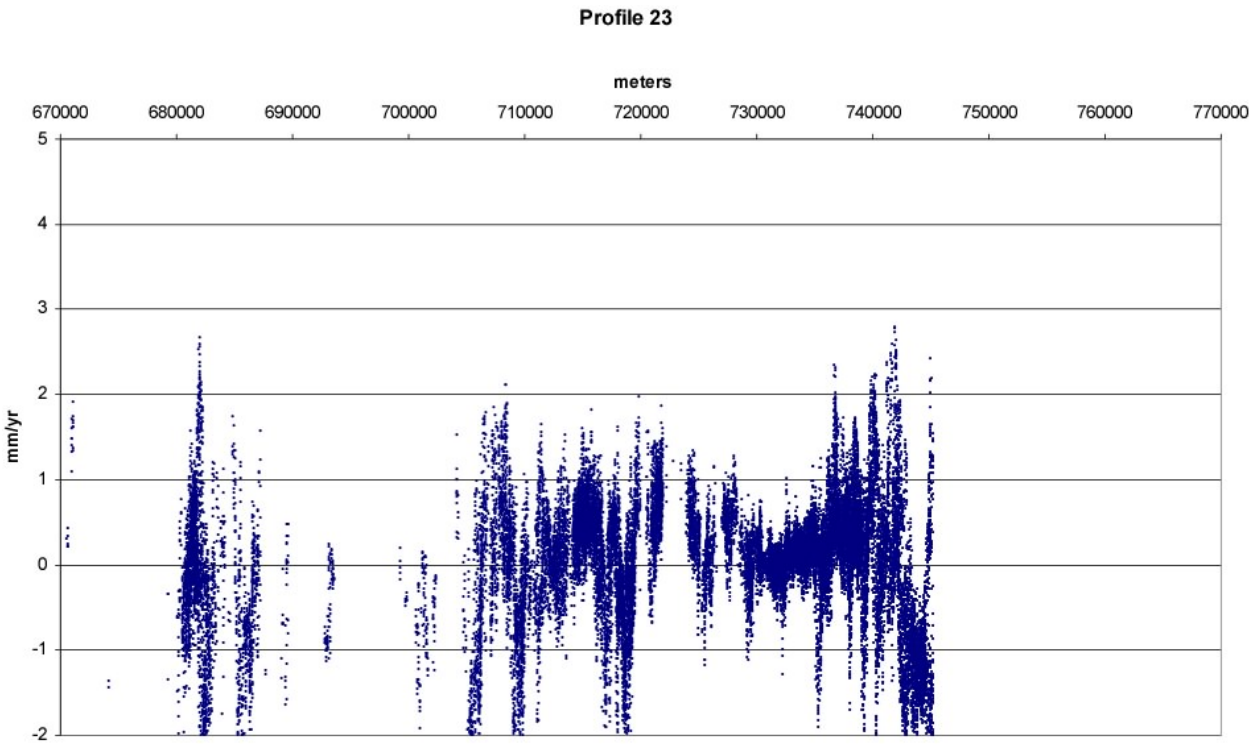

Figure DR30: Profile 23

DR item 4: Topography, landscape and rock-slope failure in the Lyngen region

The main text describes briefly the contrasting landscapes observed across Lyngenfjorden. Below, we provide DEM views and photographs that illustrate these contrasts, which appear to arise from the differential preservation of palaeosurfaces in the region. We also provide an example of a map derivative that may help to illustrate further the structural configuration around the Lyngen Peninsula.

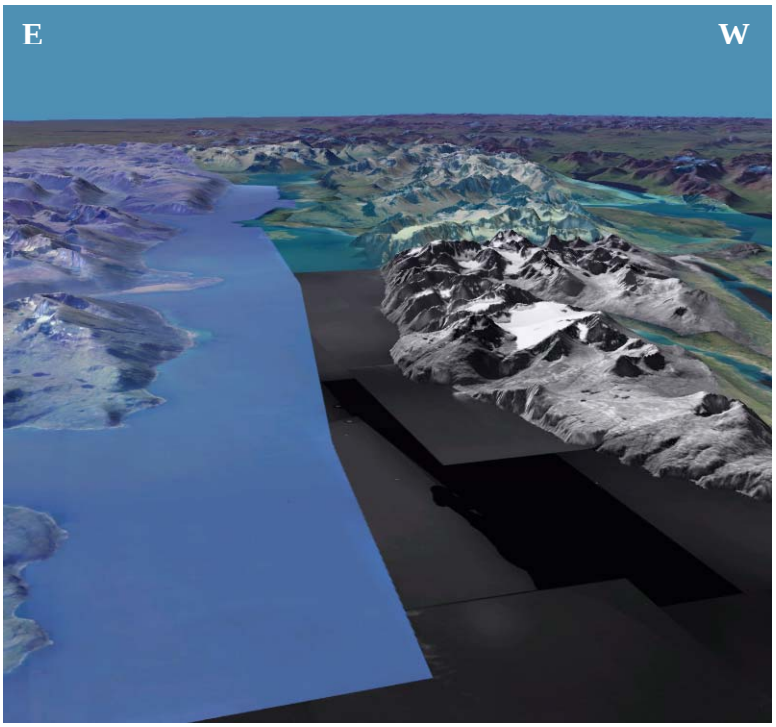

Fig. DR31.

Oblique view of DEM (www.Norgei3D.no) southwards along Lyngenfjorden, showing contrasting landscapes across the fjord. Please note that at the far (southern) end of the fjord, high topography can be traced from the southernmost part of the Lyngen peninsula (ophiolitic rocks) across to the western side of the fjord (schistose metasedimentary rocks). This indicates that topographic elevation is not universally controlled by lithology.

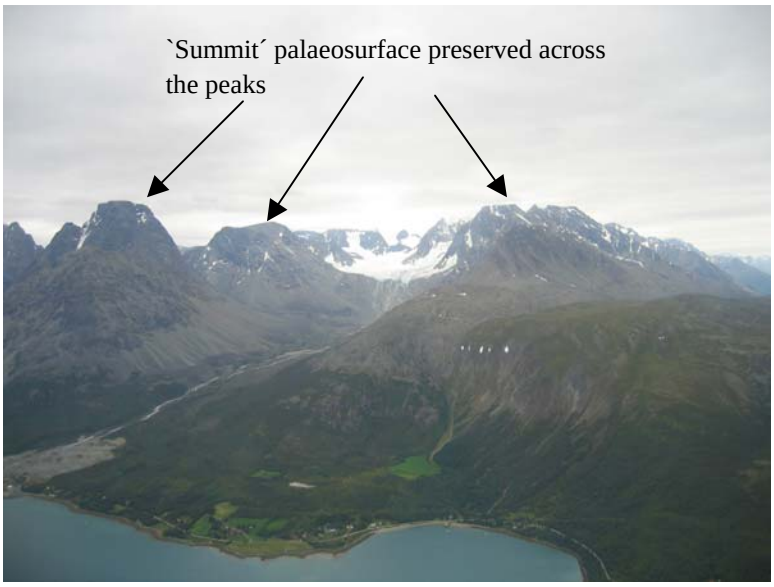

Fig. DR32.

Detail of central parts of the Lyngen peninsula, looking west, showing the `summit´ palaeosurface. In general, the deeply incised Lyngen peninsula preserves less of this palaeolandscape than the surrounding areas.

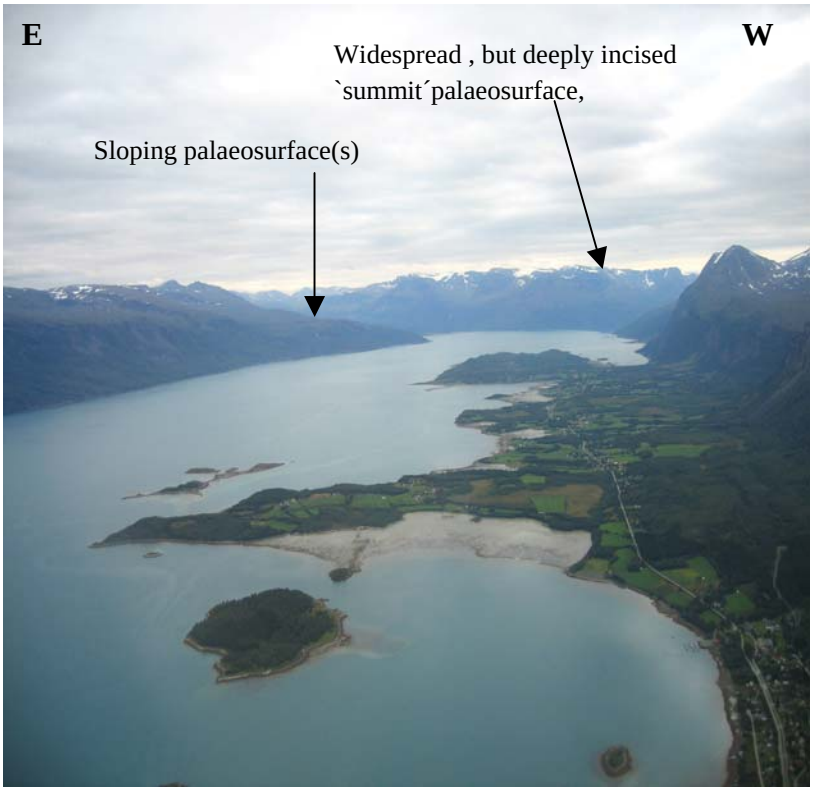

Fig. DR33.

View southwards towards southern end of Lyngenfjorden, showing contrasting landscapes across the fjord. Note high topography at south end of fjord, with relatively widespread preservation of `summit´ palaeosurface at high elevations. Towards the north, this level drops across a NW-SE-trending lineament

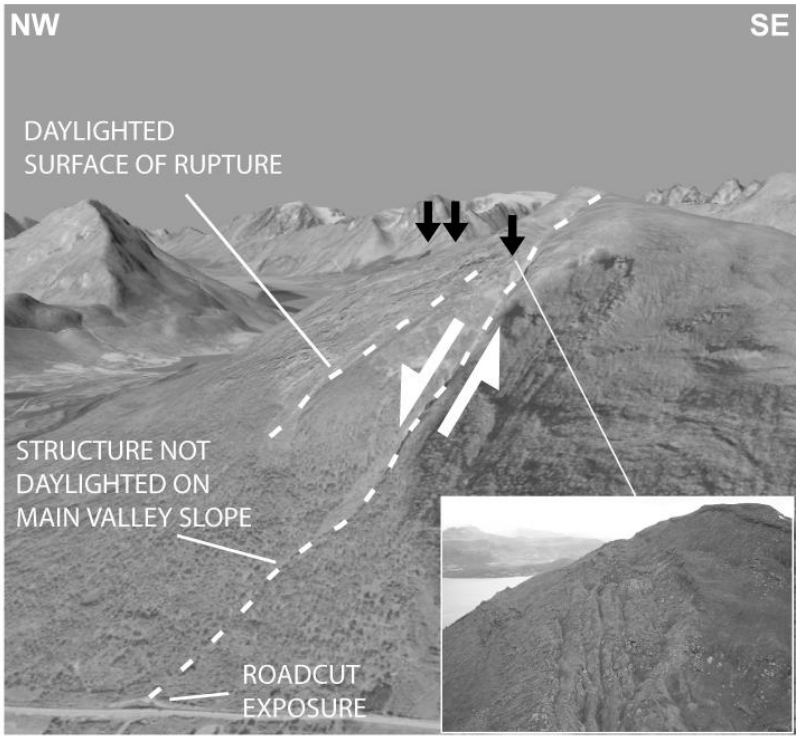

Fig. DR34.

Rockslide bund by two surfaces of rupture, inset shows multiple, scarp-bounded ridges on the northwest side of main scarp. Roadcut exposure at base of photograph is that of figure 3.d of the main text.

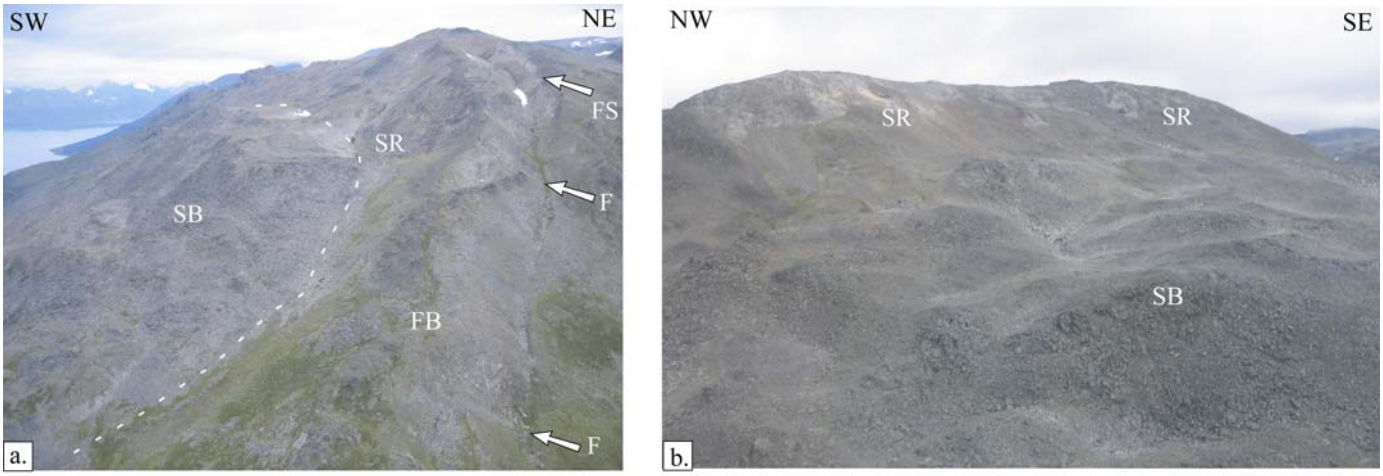

Fig. DR35.

Examples of surfaces of rupture (SR) and overlying complex rockslides, Kåfjord area. In both cases, the surface of rupture has been exhumed from underneath a complex slide containing rotated slide blocks (SB) and now constitutes the upper parts of the valley slope. In a.), another fault plane (F) is expressed as a fault scarp (FS) along the ridge, but can be traced to the floor of a tributary valley, underlying a mountain-sized fault block (FB) (see also fig. 3b in main text). Complex rockslides are developed above the surfaces of rupture, displaying various degrees of disintegration

Whereas in a.), a surface caps the uppermost slide block SB, b) presents a more dismembered and disintegrated slide, although the shape of rotated blocks can sometimes be recognised in the mounds of rubble. c.) shows slickenline lineations developed on black, polished fault surface containing a thin layer of fine-grained fault rock. This occurs on the exhumed surface of rupture close to the SE end of the photograph in b.). See stereogram in fig. 3d, main text.

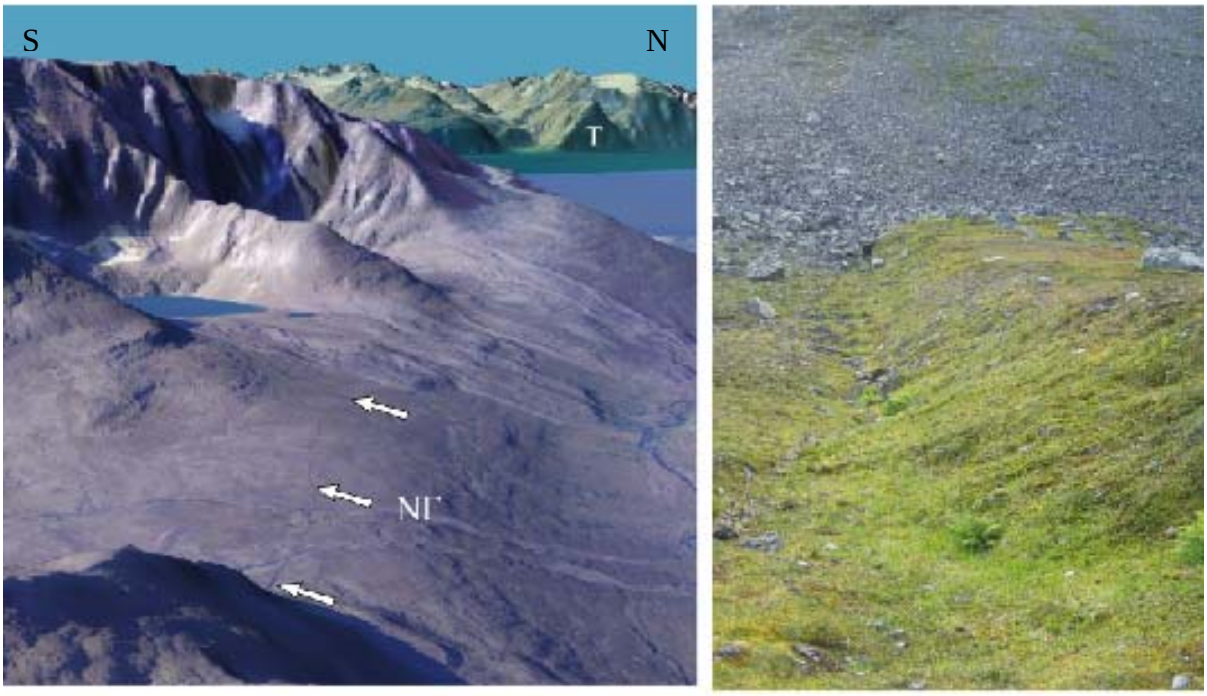

Fig. DR36

Normannvikdalen with trace of Normannvikdalen fault (NF, Dehls et al. 2000, 3-D DEM view from www.Norgei3D.no), marked by arrows. Note triangular facet (T) on the N-S-trending range front on the opposite side of Lyngenfjorden. Right-hand photograph shows the c. 2 meters high scarp in the vegetated cover along the Normannsvikdalen fault. Person for scale.

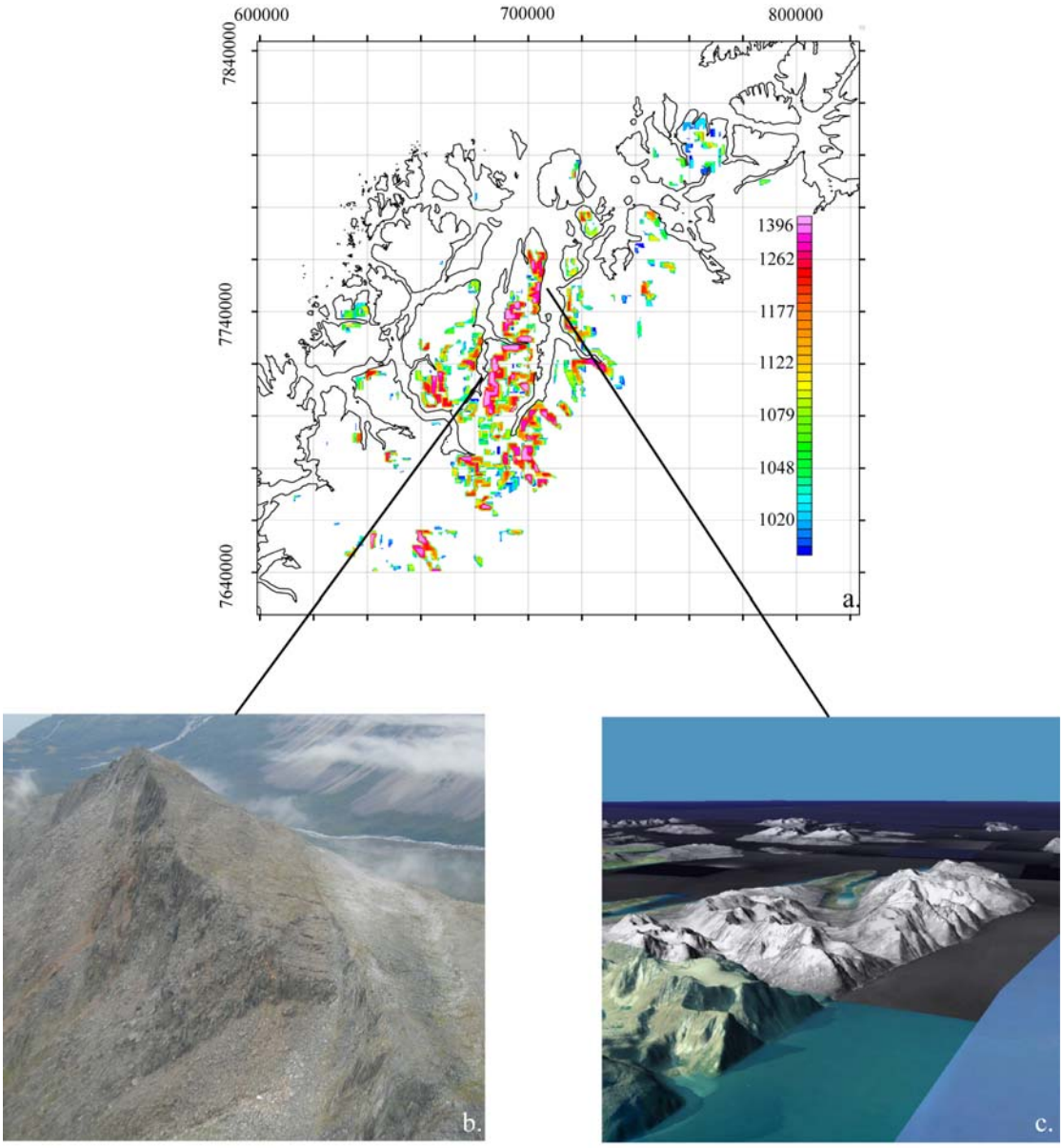

Fig. DR37.

(a) Top surface less minimum surface map of the Lyngen region. Zmax and Zmin were identified within a 3 km radius moving window passed stepwise over a 25m resolution DEM. The resultant map gives a measure of the amount of incision and the erosion potential, in this case filtered so that Zmax-Zmin > 1000m. Scale in metres. Note that the highest values are observed along the northeast and southwest sides of the Lyngen peninsula, in the areas where we have observed the faceted range-front (c) and the propagating scarps (b), respectively. This indicates that the main structures may change polarity along the peninsula, with down-to-the-east displacement in the northeast and down-to-the west displacement in the south.